Characterization of Southern Ocean Boundary Layer Clouds Using Airborne Radar, Lidar, and In Situ Cloud Data: Results From SOCRATES

Julian Schima[1,2] [ID], **Greg McFarquhar[1,2]** [ID], **Ulrike Romatschke[3]** [ID], **Jothiram Vivekanandan[3]**, **John D'Alessandro[1,2]**, **Julie Haggerty[3]**, **Cory Wolff[3]**, **Ethan Schaefer[1,2]**, **Emma Järvinen[4]** [ID], and **Martin Schnaiter[4]** [ID]

[1]School of Meteorology, University of Oklahoma, Norman, OK, USA, [2]Cooperative Institute for Severe and High Impact Weather Research and Operations, University of Oklahoma, Norman, OK, USA, [3]National Center for Atmospheric Research, Boulder, CO, USA, [4]Karlsruhe Institute of Technology, Karlsruhe, Germany

Abstract Climate and numerical weather prediction models struggle to accurately predict radiative forcing over the Southern Ocean (SO), as the amount of clouds and their phases are poorly represented in such models due to a lack of observations upon which to base parameterizations. To address this, a novel particle identification (PID) scheme, based upon airborne radar and lidar data, was applied to data collected during the Southern Ocean Clouds, Aerosol, Radiation Transport Experimental Study (SOCRATES) to assess the vertical structure of SO boundary layer clouds. A comparison between the PID scheme and in situ phase data from SOCRATES showed relatively good agreement between the two data types. The convectivity of the clouds sampled during SOCRATES was determined using the novel Echo Classification from COnvectivity for Vertically pointing radars product. The PID and in situ data were then used synergistically to identify the following features of cloud vertical structure: (a) Supercooled liquid water was very common (Probability, $P \sim 80\%$) at cloud top for convective and stratiform clouds; (b) Supercooled large drops with maximum dimensions >95 μm frequently appear within a hundred meters below cloud top, particularly within convective clouds (Max P 35%–45%), but also within stratiform clouds (Max P 20%–30%); (c) Ice production was associated with convective activity, with $P \sim 20\%$ at cloud top, increasing to 50%–70% 200 m below top, compared to $P < 30\%$ everywhere in stratiform clouds; (d) Convective clouds were found to be more vertically heterogeneous than stratiform clouds.

1. Introduction

The atmosphere above the Southern Ocean (SO) has very high cloud coverage, with the fraction of clouds below 3 km in altitude approaching 80% (Haynes et al., 2011; Mace et al., 2009). Many of these low boundary layer (BL) clouds are associated with large and complex extratropical cyclones that are prevalent over the SO (McFarquhar et al., 2021), and are one of the largest sources of disagreement among General Circulation Models (GCMs) (Bony et al., 2006; Vial et al., 2013). An understanding of the processes responsible for the complicated structure of SO BL clouds is critical for improving the parameterizations that are used to represent such processes in GCMs that model cloud radiative feedbacks in a rapidly warming global climate (McCoy et al., 2015; Tan et al., 2016; Trenberth & Fasullo, 2010), as needed to better project future climate change (IPCC, 2021).

Past studies have shown that supercooled liquid water (SLW; liquid water at subfreezing temperatures) is especially common in SO clouds, and more prevalent than at similar latitudes in the Northern Hemisphere (NH), likely due to the lack of ice nucleating particles, which tend to increase glaciation rates, over the SO (Gong et al., 2022; Kanitz et al., 2011; Radenz et al., 2021; Vergara-Temprado et al., 2018). SLW is particularly common within low clouds, although the ice phase becomes more prevalent at higher latitudes (Haynes et al., 2011; Huang et al., 2012). D'Alessandro et al. (2021) found SLW occurrence frequencies of greater than 60% for relatively low temperatures between −15 and −20°C. SLW is especially prevalent at cloud top in BL clouds (Morrison et al., 2011; Zaremba et al., 2020), and supercooled large droplets (SLD; supercooled water droplets with diameters from 100 to 500 μm, otherwise known as freezing drizzle) can also occur in SO clouds, sometimes simultaneously with ice crystals (Chubb et al., 2013; Silber et al., 2019). Within SO BL clouds, SLD frequently occurs within convective generating tops (Wang et al., 2020). SLW and SLD represent significant hazards for aircraft as they freeze on an aircraft's exterior, disrupting airflow patterns that generate lift (Cober & Isaac, 2012;

Politovich, 1989). Figure 13 of McFarquhar et al. (2021) shows an example of icing observed on cloud probes attached to the NCAR/NSF Gulfstream V (GV) aircraft during the recent Southern Ocean Cloud Radiation Aerosol Transport Experimental Study (SOCRATES) after penetrating a supercooled cloud. SLW (panel A) freezes to the aircraft relatively uniformly, while SLD (panel B) freezes in a more widespread and erratic manner; the latter pattern is more disruptive to airflow and makes SLD especially dangerous to aircraft.

Much remains unknown about the structure of SO clouds, particularly in the vertical dimension (Haynes et al., 2011; McFarquhar et al., 2021) as passive remote sensing instruments, with the exception of microwave sounders, only retrieve vertically integrated or cloud top properties. Active sensors (e.g., radar and lidar) can be used to retrieve vertical cloud structure (e.g., Bodas-Salcedo et al., 2016; Bony, 2007; Shupe, 2007), but such retrievals are not well evaluated over the SO due to a lack of in situ data (McFarquhar et al., 2021). The lack of evaluation data is problematic due to inherent uncertainty present in remote sensing retrievals, such as distinguishing between ice crystals and SLD, the attenuation of radar and lidar signals (Chubb et al., 2013; Huang et al., 2012), and the relatively low solar zenith angles.

The 2018 SOCRATES field experiment obtained an extensive set of collocated in situ and remote-sensing data over the SO that can be used to evaluate remote-sensing retrievals (McFarquhar et al., 2021). The mission consisted of 15 research flights of an NCAR/NSF GV aircraft, equipped with airborne radar, lidar and in situ cloud probes, over the Australasia sector of the SO in the cold sectors of extratropical cyclones where GCMs have historically struggled to show sufficient SLW to produce the observed shortwave fluxes (McFarquhar et al., 2021; Mülmenstadt et al., 2021). This consistent modeling error has led to an underestimate of cloud albedo, as liquid-phase clouds are more reflective than ice-phase clouds due to their larger optical depth (Cheng et al., 2012; Mülmenstadt et al., 2021). As a result, the potential feedback response of SO BL clouds to global warming remains uncertain (e.g., Bodas-Salcedo et al., 2016; McFarquhar et al., 2021; Mülmenstadt et al., 2021).

A major reason for the failure of GCMs to produce sufficient SLW is their poor performance in simulating the commonly occurring mixed phase and supercooled clouds within the SO BL (Bodas-Salcedo et al., 2014; Komurcu et al., 2014; McCoy et al., 2015). Within mixed-phase clouds, ice crystals grow at the expense of supercooled drops by the Wegener-Bergeron-Findeisen (WBF) process, due to the lower saturation vapor pressure of ice relative to liquid water (e.g., Cesana et al., 2015; Fan et al., 2011; Storelvmo & Tan, 2015; Storelvmo et al., 2008; Tan & Storelvmo, 2016). Models typically assume homogeneous mixtures of liquid and ice within a model gridbox (Fan et al., 2011; Storelvmo et al., 2008). However, in reality, mixed-phase clouds typically show significant heterogeneity within a single model gridbox, with areas of predominantly liquid and areas of predominantly ice both present (Chylek & Borel, 2004; D'Alessandro et al., 2021; Korolev & Isaac, 2003; McFarquhar & Cober, 2004). This inconsistency likely leads models to overestimate the efficiency of the WBF process (Tan et al., 2016), especially over the SO where SLW is prevalent. Aside from the WBF process, inaccurate parameterizations of primary and secondary ice production (SIP) produce further inaccuracies in SLW estimations in the models (Field et al., 2017).

Over the SO, attempts to correct modeling errors by forcing GCMs to generate more SLW have been somewhat successful by imposing the presence of SLW at lower temperatures (Kay et al., 2016). However, the processes for the production of this SLW have not been established, and the addition of SLW has exposed new errors in the models and worsened their representation of the current climate (Mülmenstadt et al., 2021). It is clear that adjusting a single parameter is insufficient for correctly modeling SO clouds, and thus a complete understanding of the basic structure of SO clouds and the interaction of particles within them is required (McCoy et al., 2015; Stephens, 2021; Tan et al., 2016). The use of high resolution remote sensing data from SOCRATES can thus have important applications.

This study applies a novel particle identification (PID) scheme to in-flight radar data collected during SOCRATES to retrieve vertical profiles of cloud phase and the presence of SLD. Evaluation of the PID scheme is performed by a comparison against in situ observations where remote sensing and in situ data were collected in close proximity during ramped ascents and descents of the GV through BL clouds. Finally, the composite in situ and PID data are used to derive information about common vertical structures of SO BL clouds.

The remainder of this paper is organized as follows. Section 2 discusses evaluation of cloud phase from both in situ and remote sensing data. Section 3 analyzes four case studies of vertical BL cloud structure using ramped ascents and descents through clouds. Section 4 compares the results of the PID scheme to the in situ observations.
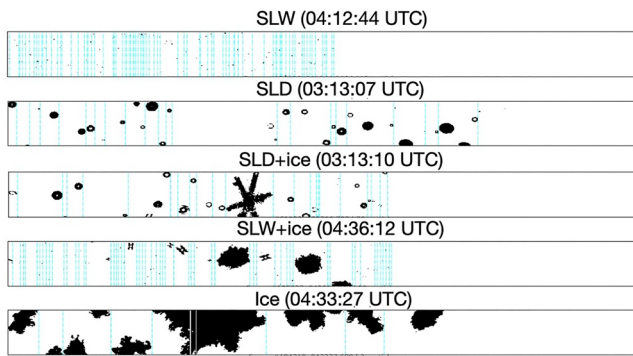
Figure 1. Selected 2D-S images from 5 February, with phase and time labeled. The vertical scale of each plot is 1.28 mm, and each individual pixel has dimensions of 0.01 mm × 0.01 mm.

Finally, Section 5 shows the use of in situ and remote sensing data to quantitatively assess the typical vertical structure of SO BL clouds.

2. Cloud Phase Classification

2.1. In Situ Data

This section discusses methods of identifying cloud phase using both the in situ and remote-sensing data, and compares the identified phases for collocated remote sensing and in situ observations. Detailed information about the in situ and remote probes installed on the NCAR/NSF GV during SOCRATES, their operating characteristics, and the algorithms used to process the data are discussed elsewhere (e.g., D'Alessandro et al., 2021; Järvinen et al., 2022; McFarquhar et al., 2021; Wang et al., 2020; Zaremba et al., 2020, 2021). Thus, only a brief summary is provided here together with a focus on unique aspects of the processing required for this analysis.

The probes used for determining in situ phase include the Cloud Droplet Probe (CDP) (Lance et al., 2010), the 2-Dimensional Stereo Probe (2D-S) (Lawson et al., 2006), the airborne Particle Habit Imaging and Polar Scattering probe (PHIPS) (Abdelmonem et al., 2016; Schnaiter, 2018; Waitz et al., 2021), and the Rosemount Icing Detector (RICE) (Baumgardner & Rodi, 1989; Cober et al., 2001). A Two-Dimensional Optical Array Cloud Probe (2D-C) was also mounted on the NSF/NCAR GV (Jensen & Stith, 2021), but often experienced fogging issues, so its data were not used to generate the base phase distributions (D'Alessandro et al., 2021; McFarquhar et al., 2021). However, 2D-C data were used for a segment of one research flight, RF08 from 03:10 to 04:42 UTC, when the 2D-S probe experienced a problem with stuck bits (McFarquhar et al., 2018) after additional analysis (see Appendix A) suggested the 2D-C data were not contaminated by fogging during that flight segment.

D'Alessandro et al. (2021) combined data from the 2D-S, RICE, and CDP to produce a cloud phase product for SOCRATES. Cloud phase is characterized as no cloud, liquid, mixed (liquid and ice), or ice phase for all in-flight observations at a frequency of 1 Hz for air temperatures less than 0°C using a machine-learning algorithm. Representative images of cloud particles obtained by the 2D-S for time periods identified with the indicated cloud phase are shown in Figure 1. Note that SLW is characterized by numerous very small particles on the 2D-S, while larger round particles are typical of SLD. The larger round particles frequently appear donut-shaped because many drizzle sized drops are outside the 2D-S depth of field. Ice crystals typically appear as large, irregularly shaped (non-round) particles. A schematic showing the scheme used to identify cloud phase is displayed in Figure 2 of D'Alessandro et al. (2021).

As machine learning algorithms are not without error, the phase product was carefully evaluated and improved for use in this study. First, a manual assessment of particle images from the 2D-S, 2D-C, and PHIPS probes was performed. Although the images do not determine phase on their own, since many water droplets are too small to be imaged, and probe resolution makes it difficult to distinguish the shapes of small ice crystals from small droplets (e.g., McFarquhar et al., 2013), images of larger particles can be used to correct errors, including a misclassification of precipitating drizzle as ice crystals that sometimes occurred in the D'Alessandro et al. (2021) product. In addition, there were time gaps in the D'Alessandro et al. (2021) product from time periods when the 2D-S was not available (e.g., during RF08 on 4 February 2018 when data were not available for some of the boundary-layer cloud sawtooths, which are instances where the GV repeatedly ascended and descended through a cloud layer). For these periods, particle images from the 2D-C and PHIPS probes were used to identify the phase of the larger particles, and then in combination with the RICE and CDP data the phase of each 1 s period was determined following the D'Alessandro et al. (2021) algorithm. Although there is uncertainty in the use of the 2D-C to quantify concentrations and particle sizes due to fogging on the diodes, the images are of sufficient quality to manually determine phase.

In total, out of 313,125 1 s in-flight observations (with temperature below 0°C) used by D'Alessandro et al. (2021), 6,390 observations (2.04%) had the predicted phase modified, with a net increase of 1,720 "in-cloud" observations (0.55%). Of further note is that 4.4% of ice-phase observations were reclassified as liquid, with almost no liquid observations reclassified as ice. A full comparison of the changes is provided in Figure 2.

Phase (new product)

	N	L	M	I
N	266705 (85.17%)	797 (0.25%)	446 (0.14%)	1243 (0.40%)
L	184 (0.06%)	21639 (6.91%)	705 (0.23%)	7 (<0.01%)
M	39 (0.01%)	673 (0.21%)	3148 (1.01%)	865 (0.28%)
I	543 (0.17%)	737 (0.24%)	151 (0.05%)	15243 (4.87%)

Phase (old product) (vertical axis label)

Figure 2. Comparison of cloud phase for original and modified versions of in situ phase product from D'Alessandro et al., 2021. Abbreviations: N, no cloud; L, liquid; M, mixed; I, ice. The shaded diagonal indicates where phase was unchanged. Number in top row indicates number of observations with indicated new phase product (vertical) and old phase product (horizontal). Number in parentheses indicates percentage of the total number of observations in that category (raw total/313,125).

SLD was distinguished from SLW using a minimum concentration of liquid particles above a particular size measured by the 2D-S probe. One of the only previous studies to use such a threshold was that of Cober and Isaac (2012). They identified the presence of SLD as 30 s time periods when 10 or more particles with maximum dimension (D) >100 μm were detected by a 2DC. In order to apply this definition to the 1 s SOCRATES data, the sampling areas of the 2D-S and 2D-C were used to determine that the Cober and Isaac (2012) definition was equivalent to a number concentration of particles with $D > 100$ μm greater than 8.5×10^{-2} L^{-1} measured by the 2D-S. However, since the 2D-S data were processed so that there was a bin containing particles with $95 < D < 105$ μm, a threshold of $D = 95$ μm was used for the smallest particles representing SLD. For reasons discussed in Section 4, the threshold concentration used to define SLD was increased to 1 L^{-1} to better match the identification of SLD from the remote sensing data. In liquid-phase conditions, the concentration of all 2D-S particles with $D > 95$ μm was used, as all particles were assumed to be liquid, while in mixed-phase conditions, the concentration of only round 2D-S particles with $D > 95$ μm was used, as the non-round particles were likely ice.

Although SLD and ice were observed concurrently on numerous occasions (based on 2D-S and PHIPS images), the concentrations of round and non-round particles included in the 2D-S data set (Wu & McFarquhar, 2019) do not correspond to concentrations of liquid and ice-phase particles respectively. Some ice crystals are inevitably included in the round concentrations since there are variations in both the shapes and orientations of the ice particles that are imaged. Thus, it is assumed that SLD was not present when the ratio of the concentration of round particles to that of all particles ($D > 95$ μm) was less than 0.3 in mixed-phase conditions. Although some uncertainty exists in the 0.3 threshold used to identify SLD, results were generally consistent when compared with manual phase observations in the case studies described in Section 3.

While in situ data used in this study were determined at 1 s resolution, a 3 s rolling average was applied in order to have a more statistically significant sample of particles for identifying phase than could normally be obtained with 1 s resolution (e.g., McFarquhar et al., 2007). This is 10 times finer resolution than used by Cober and Isaac (2012), and is necessary to capture the fine-scale heterogeneity in phase observed by Wang et al. (2020) for the generating cells present near the tops of these BL clouds. They noted the average widths of these generating cells that contained more SLW than surrounding areas was 395 m, which corresponds to about 3 s of penetration by the NSF/NCAR GV aircraft.

2.2. Remote Sensing Data

Airborne remote sensing data were collected by the High-Performance Instrumented Airborne Platform for Environmental Research Cloud Radar (HCR) and by the High Spectral Resolution Lidar (HSRL). The HCR is an airborne, dual polarimetric millimeter-wavelength cloud radar with a vertical resolution of about 19 m and temporal resolution of 10 Hz; the HCR, its calibrations, and the processing of the SOCRATES data are described in Vivekanandan et al. (2015), Rauber et al. (2017), and Romatschke et al. (2021). The HSRL (Albrecht et al., 2019; Eloranta et al., 2008; Schwartz et al., 2019) is a calibrated lidar that uses a high-repetition, low pulse-energy laser. Zaremba et al. (2020) describes its use during SOCRATES. The sample rate of the HSRL is 2 Hz, with vertical range resolution of 7.5 m (Romatschke & Vivekanandan, 2022).

Romatschke and Vivekanandan (2022) describe the development of a remote-sensing based particle-identification (PID) scheme that uses data from the HCR and HSRL. As boundaries between particle types within clouds generally are not sharply and clearly defined, the PID scheme employs a fuzzy-logic algorithm to determine particle type. HCR parameters used in the scheme are reflectivity, Doppler velocity, linear depolarization ratio (LDR), and temperature, with the HSRL linear depolarization ratio (LLDR) and backscatter coefficient also incorporated.
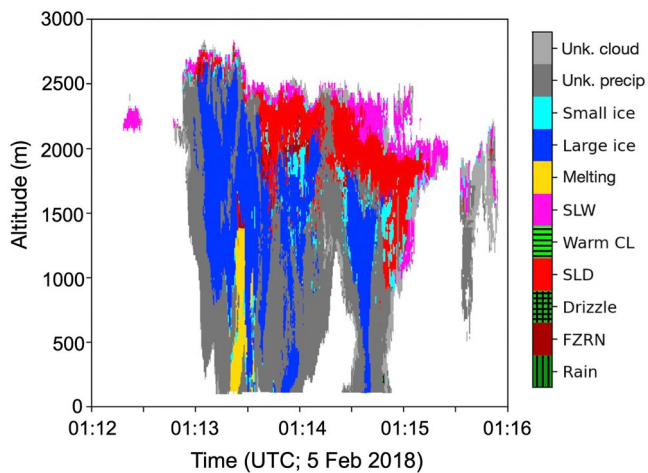
Figure 3. Phase retrieved by the particle identification scheme between 01:12 and 01:16 UTC for RF09 on 5 February 2018, color coded by particle type.

Supercooled liquid particles were classified by particle size as freezing rain (FZRN), SLD, or SLW, with respective warm liquid categories also present. Ice phase particles were simply classified as either small or large. A "melting" classification indicates melting frozen precipitation at above-freezing temperatures. However, if it appears in below-freezing temperatures, it represents a mix of SLD and ice. As LDR and LLDR are especially important for particle type classification and as the HSRL can be easily attenuated, areas without either LDR or LLDR were assigned an unknown phase ID as "cloud" if smaller particles were observed and "precipitation" when larger particles were present.

An example of the PID retrieval for a supercooled boundary-layer cloud sampled on RF09 between 01:12 and 01:16 UTC on 5 February 2018 is shown in Figure 3. With an approximate airspeed of 150 m s^{-1}, this corresponds to a horizontal distance of about 36 km. The data upon which these retrievals are based were collected on an outbound leg from Hobart toward the Antarctic (at a latitude around 53°S) when the GV was flying at ~7 km altitude with the radar pointing down. The scheme shows a 50–300 m thick layer of SLW in pink near cloud top, particularly between 01:13:30 and 01:15 UTC, with a 300–400 m thick layer of SLD in red below. Glaciation and a transition to large ice as precipitation is seen at an altitude of 1,700–2,000 m between 01:13:30 and 01:15 UTC, with the gray colors indicating uncertainty in precipitation type at heights below 2 km due to the attenuation of the lidar. Less layering was seen between 01:13:00 and 01:13:30, where mostly large ice was present. The retrievals terminate about 100 m above sea level, as the lowest five bins of data above the ocean surface were masked due to impacts from sea spray (Romatschke et al., 2021).

The impact of convection on vertical cloud structure is examined in this study. To quantify convective activity (convectivity), the novel Echo Classification from COnvectivity for Vertically pointing radars (ECCO-V) product, based on HCR data, is used (Romatschke & Dixon, 2022). This algorithm uses a combination of averaged radar reflectivity and radial velocity to classify the convectivity of cloud regions as stratiform, convective, or a mix of stratiform and convective elements. The algorithm was shown to be skilled at identifying localized embedded convective features in addition to isolated convective or stratiform regions, based on analysis of case studies from the SOCRATES and Organization of Tropical East Pacific Convection field campaigns (Fuchs-Stone et al., 2020; Romatschke & Dixon, 2022). This is particularly useful in the context of SOCRATES, where convective elements frequently were embedded in larger stratocumulus decks.
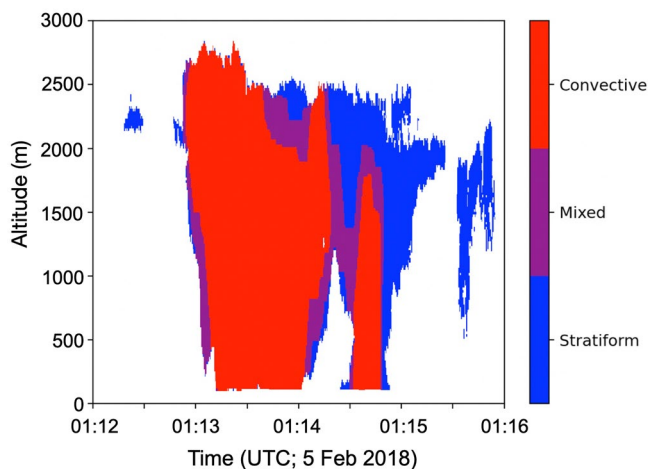
The ECCO-V classification for the same cloud region and time period as in Figure 3 is shown in Figure 4. The cloud region was identified to be mostly convective, indicated by the red shaded regions, although a portion of cloud between 01:14 and 01:16 UTC and mostly above 1.5 km in altitude is labeled as stratiform. Mixed convective and stratiform characteristics are shown along the interface of most convective and stratiform regions.

3. Cloud Case Studies

Four examples of the observed vertical structure of BL clouds are discussed in this section using data collected during ramped ascents/descents through clouds in the BL. These case studies are also used to highlight some of the similarities and differences between the PID and in situ identified phase. Two of the case studies represent predominantly stratiform conditions, while the other two cases are more convective. The stratiform cases show both thin and thick clouds, while the convective cases display different amounts of in-cloud glaciation.

Figure 5 shows data collected during the ascent of the NSF/NCAR GV during RF14 on 22 February 2018 between 03:36 and 03:45 UTC. A very
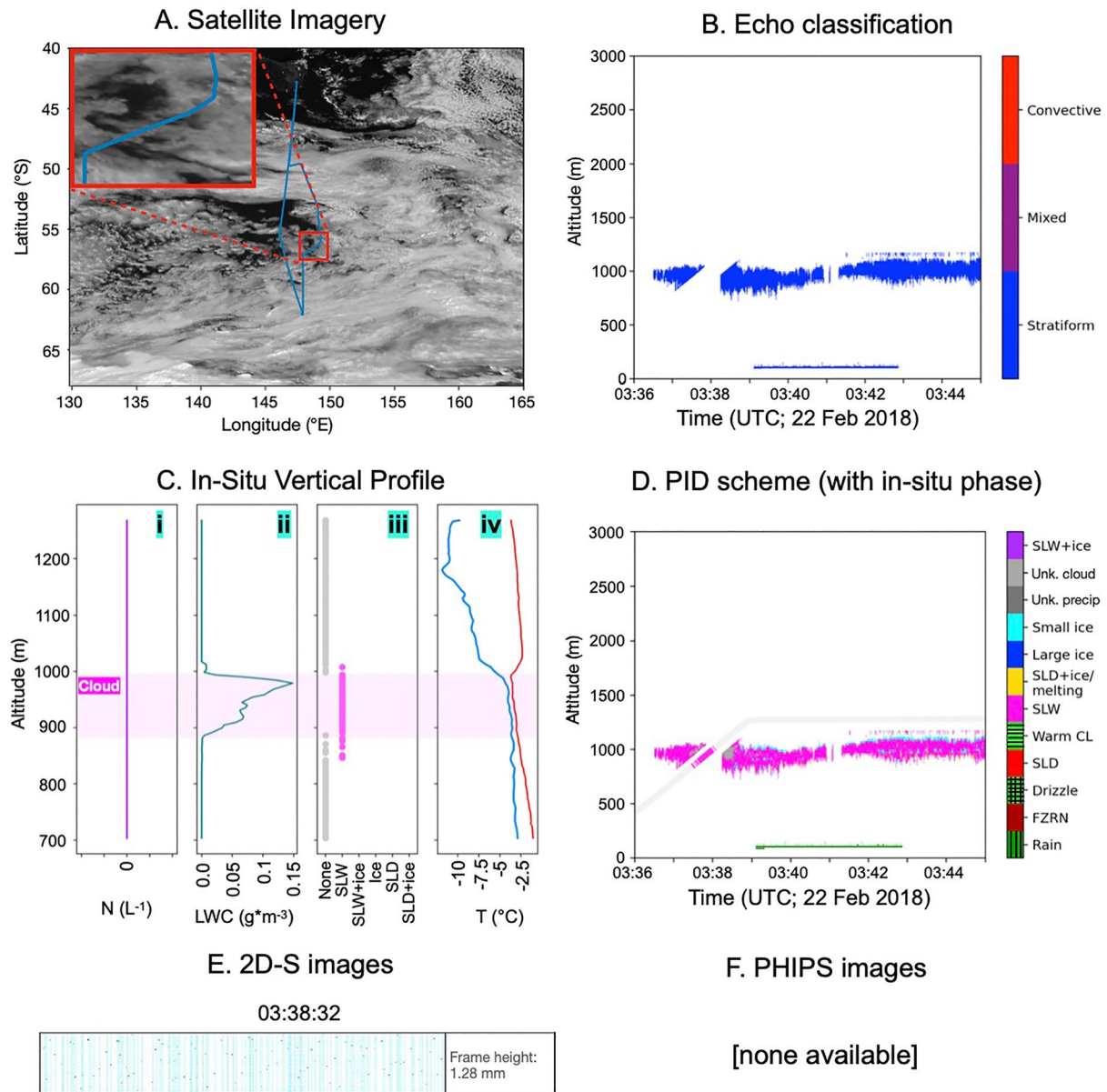

Figure 4. Echo Classification from COnvectivity for Vertically pointing radars classifications between 01:12 and 01:16 UTC for RF09 on 5 February 2018, showing areas of stratiform and convective activity.

Figure 5. Cloud case study, 03:36–03:45 UTC, 22 February 2018. (a) Black and white HIMAWARI satellite image at 03:40 UTC, with the approximate cloud location in the red box, and the flight track in blue. (b) Echo Classification from COnvectivity for Vertically pointing radars classifications deduced from the High-Performance Instrumented Airborne Platform for Environmental Research Cloud Radar and High Spectral Resolution Lidar data. (c) Vertical profile of in situ measurements plotted against altitude (i: 2D-S concentrations of particles with $D > 95$ μm (none observed), ii: liquid water content from Cloud Droplet Probe (CDP), iii: in situ phase following the modified D'Alessandro et al. (2021) algorithm, iv: temperature (red) and dewpoint (blue). (d) Phase derived from particle identification scheme (colors) together with in situ derived phase colored on line representing altitude variation of GV aircraft. (e) Representative 2D-S images from the cloud (time refers to when the first image in the frame was taken), (f) no images were recorded with the Particle Habit Imaging and Polar Scattering probe probe. The liquid water path from the CDP was 8 g m^2.

thin layer (thickness 100–200 m) of fair-weather stratocumulus was present, with breaks in the cloud visible on satellite (Figure 5a). ECCO-V shows the cloud to be fully stratiform, as indicated by blue color (Figure 5b). Figure 5ci indicates virtually no large particles with $D > 95$ μm (whether ice or SLD) were present. Figure 5cii shows that the liquid water contents measured by the CDP were less than 0.15 g m^{-3}, which is quite small compared to that sampled during other penetrations and suggests there was not sufficient liquid water to initiate the collision-coalescence process to produce SLD. The in situ phase shown in Figure 5ciii is exclusively SLW and the in-cloud temperature averaged −3°C as shown in Figure 5civ. It can further be observed that 2D-S images consisted of small round particles, typical of SLW (Figure 5e), and no PHIPS images were obtained.

Since the PHIPS only images aspherical particles with $D > 20$ μm and spherical particles with $D > 60$ μm (Waitz et al., 2021), this indicates few (<0.02 L^{-1}) or no large particles were present.

The pink-colored retrievals from the PID in Figure 5d suggest that almost exclusively SLW was present, in agreement with in situ data, although a few "small ice" retrievals can be seen in light blue along the cloud top; the lack of ice in the in situ data and lack of vertical coherence in the "small ice" retrievals suggests that the identification of "small ice" at cloud top is an artifact of the algorithm that occurs due to weak HCR/HSRL returns at cloud top. The in situ observations are shown in Figure 5d in the form of a color-coded line following the aircraft's altitude, which cuts through the PID retrievals at around 03:38 UTC. A gap in the availability of the PID around the location of the aircraft is caused by the ~100 m zone of invalid data around the radar due to near-aircraft effects (Romatschke & Vivekanandan, 2022).

Overall, the cloud layer shown in Figure 5 is homogeneous, with no precipitation occurring. A temperature inversion and quickly widening dewpoint depression seen at cloud top (in Figure 5civ), representing the top of the atmospheric BL, likely capped the cloud growth. The structure seen in Figure 5 was very typical for thin stratiform clouds observed during SOCRATES, with multiple similar examples present in both the in situ and remote sensing data.

A thicker (~650 m thick) cloud deck is shown in Figure 6. Figure 6a shows the location of the cloud deck near 60°S, in the northwest quadrant of a large extratropical cyclone. Figure 6b shows the cloud is predominantly stratiform, although a single convective cell was present around 02:06 UTC. Figure 6cii shows larger values of liquid water content (LWC) than shown for the thinner stratiform cloud in Figure 5, with LWCs frequently exceeding 0.3 gm^{-3}. In situ phase (Figure 6ciii) indicates that the cloud was fully liquid, with the large particles on the 2D-S (Figure 6ci) being circular and those on the PHIPS (Figure 6f) having smooth edges and a Poisson spot, both indicating SLD. The non-spherical shape in case of the larger droplets is caused by deformation of the droplets in the instrument's inlet. Three vertically adjacent regions of the cloud are noted. In region 1 (near cloud top, between 1,400 and 1,100 m altitude and 02:01–02:07 UTC), SLW is present but not much SLD. In region 2 (bottom portion of cloud between 1,100 and 700 m altitude and 02:01–02:06 UTC), both SLW and SLD are present. In region 3 (below cloud, <700 m altitude and 02:01–02:05 UTC), the LWC drops to near zero and a notable T/Td spread emerges (Figure 6civ), suggesting the retrievals correspond to below cloud base where some evaporation could be occurring. However, SLD is still present as precipitation.

Near and below cloud base, the PID shows similar results to the in situ data, showing patches of SLD lining up with the highest SLD concentrations in situ, and SLW elsewhere (Figure 6d). However, in region 1, the PID could not determine cloud phase because lidar measurements were unavailable (with no LDR data available from the HCR either). A few pixels of "small ice" appear in the area of unknown phase between 1,000 and 1,400 m between 02:01 and 02:07 UTC; but these appear erroneous due to the lack of any ice in the in situ observations. This phenomenon can also be seen in Figures 7d and 8d, and could lead to an overestimation of ice phase by the PID.

Figure 7a shows a cloud region near 55°S with a maximum thickness of at least 1,200 m (see Figure 7b). Data from the 2DC probe were used to quantitatively characterize the cloud due to an issue with stuck bits on the 2D-S for this time period. A plot supporting the validity of using the 2DC data for a portion of this flight is provided in Appendix C. As annotated in Figure 7c, the plane first flew through a developing convective cell from 04:15 to 04:16 UTC, which extended vertically from around 400 m to about 1,000 m based on combined in situ and remote sensing data (region 3 in Figures 7c and 7d), then a more developed convective cell from 04:16 to 04:18 UTC, with cloud base below 800 m (exact height unknown due to lack of data), and cloud top around 1,800 m (region 2 in Figures 7c and 7d).

Note that although the cell in region 3 is labeled as stratiform in Figure 7b, the HCR Doppler velocity (not shown) upward motion exceeded 2 ms^{-1}, indicating some convective activity. However, the very early stage of development of this cell was not sufficient to justify a "convective" classification due to small HCR reflectivity values of 10 dBZ or less and the small extent of the cloud (Romatschke & Dixon, 2022). Both cells contained ice crystals, with relatively small LWC values of 0.1–0.15 g m^{-3}. Figure 7ciii shows SLD + ice in region 2 based on concentrations of large round particles up to 15 L^{-1} on the 2D-S (round particle concentrations not shown), but 2DC and PHIPS images (Figures 7e and 7f) do not show any SLD in the region (instead showing ice crystals in the form of rimed needles, needle aggregates, and faceted shapes), so it is assumed that all the large particles seen in Figure 7ci are ice crystals.
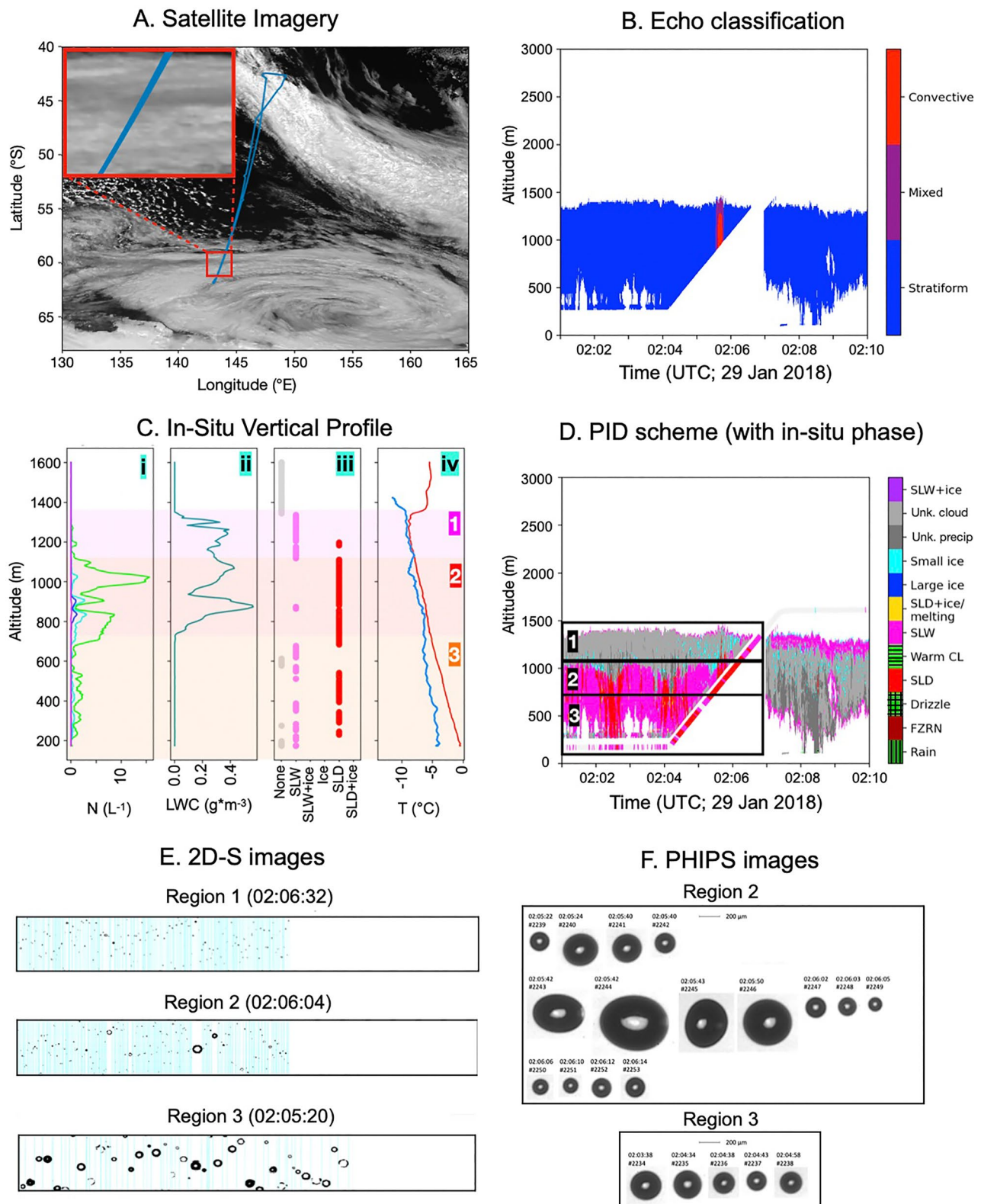
Figure 6. Cloud case study, 02:01–02:10 UTC, 29 Jan 2018. Panels are as described in Figure 5, with a satellite image from 02:00 UTC. In panel Ci, 2D-S concentrations of particles with $D > 95$, 195, 295, and 495 µm are shown in green, light blue, blue, and purple, respectively. No images were recorded on the PHIPS in labeled region 1. The liquid water path was 164 g m^{-2}.
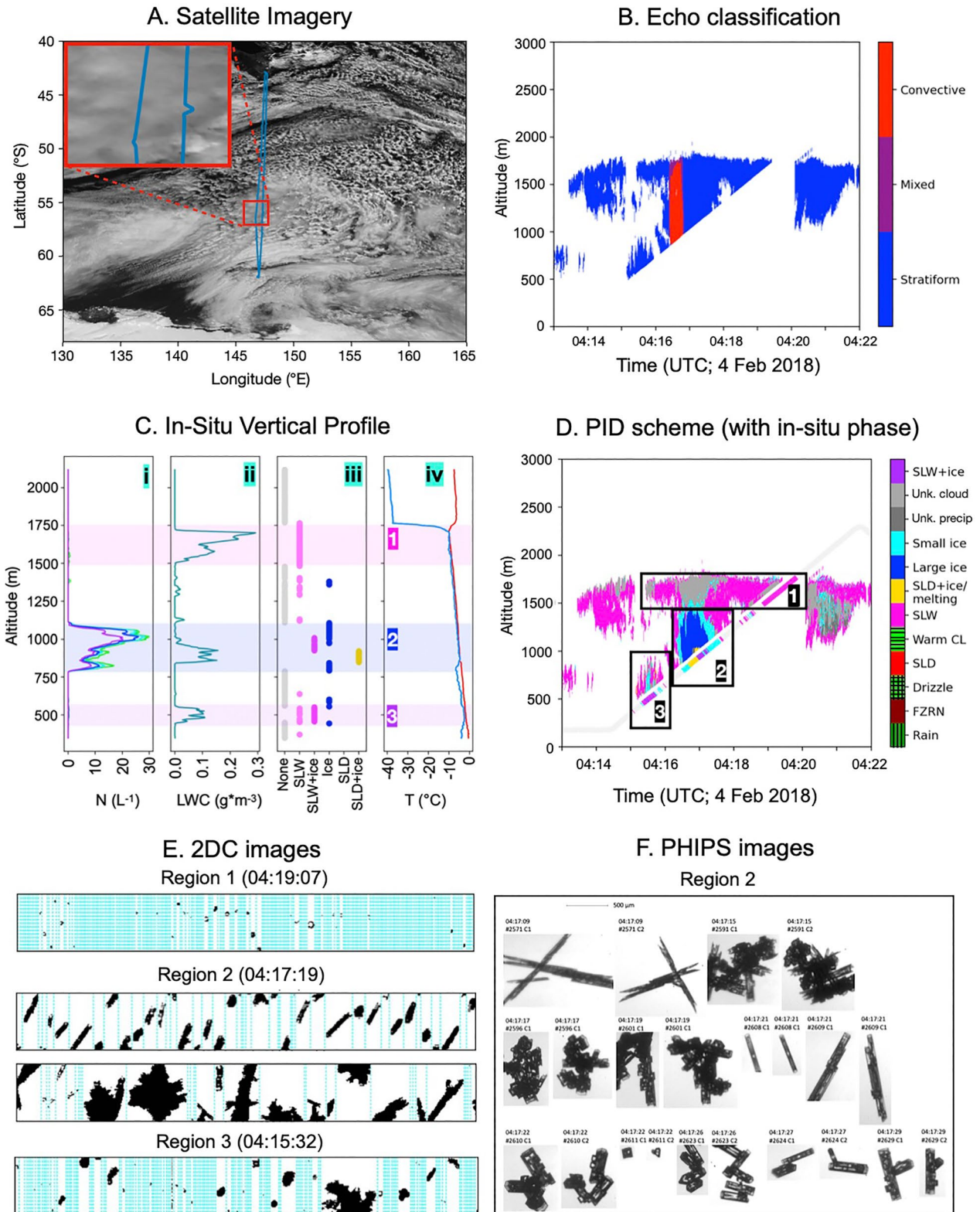
Figure 7. Cloud case study, 04:13–04:22 UTC, 4 Feb 2018. Panels are as described in Figure 6, with a satellite image from 04:20 UTC. All in situ "ice" is labeled in light blue in panel (d), since no large versus small ice classification exists in situ. No images were recorded on the Particle Habit Imaging and Polar Scattering probe in labeled regions 1 and 3. The liquid water path was 51 g m^{-2}.
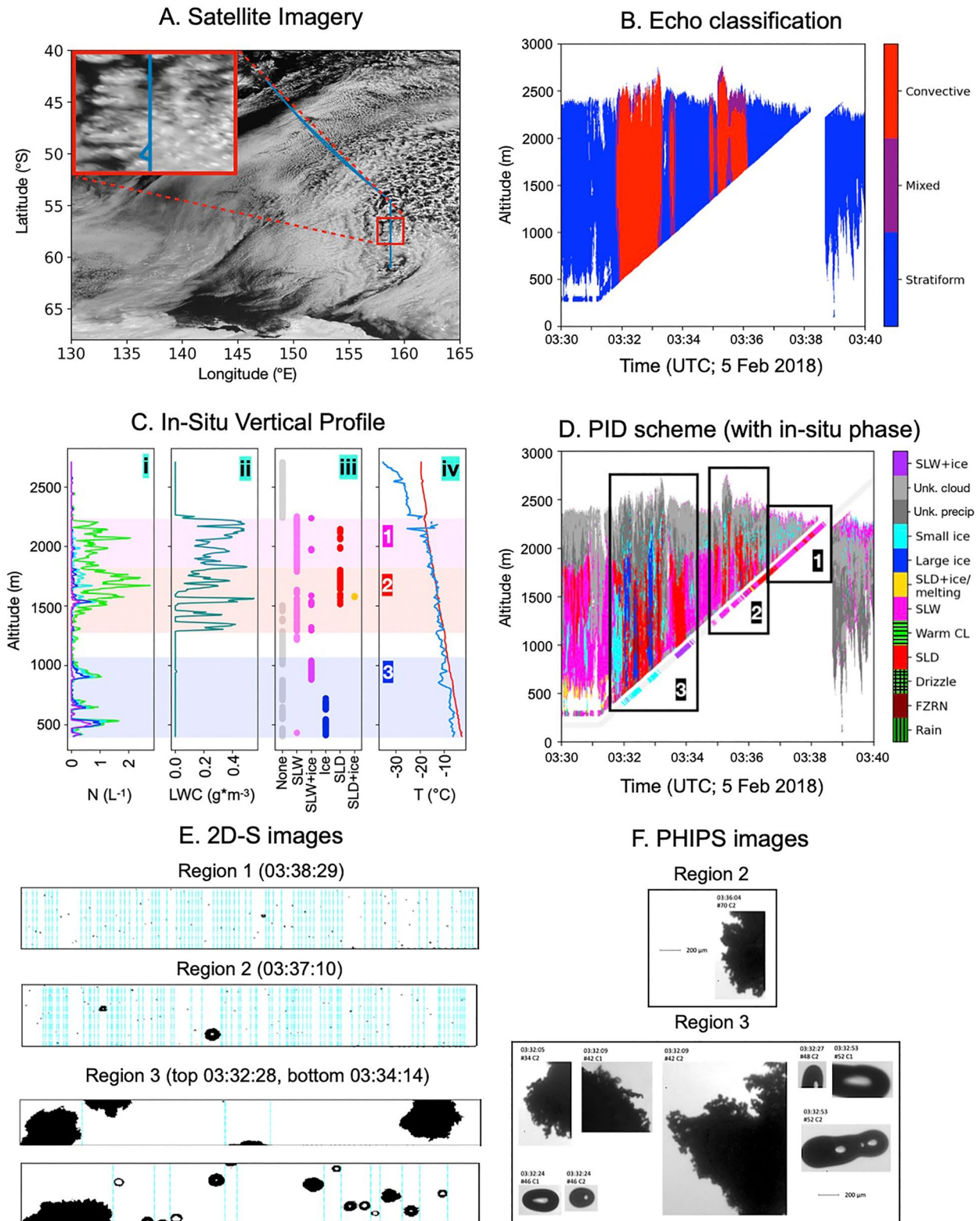
Figure 8. In situ and remote sensing data from 03:30 to 03:40 UTC, 5 Feb 2018. Panels are as described in Figure 6, with a satellite image from 03:30 UTC. No images were recorded on the Particle Habit Imaging and Polar Scattering probe in labeled region 1. The liquid water path was 217 g m^{-2}.

The PID scheme showed similar results (Figure 7d), with "large ice" determined for time periods when the in situ observations (Figure 7ci) showed many large ice crystals (~20 L^{-1} for particles with $D > 495$ μm) in region 2, and "small ice" where smaller concentrations of ice crystals (<1 L^{-1} for crystals of any size) existed in region 3. Note that there is no category of "SLW + ice" in the PID scheme because the larger ice crystals will make larger contributions to the radar reflectivity than the smaller water drops, so the "large ice" retrievals seen in region 2 are consistent with the in situ data.

Next, the GV flew through a higher cloud deck consisting of SLW (as indicated in Figure 7ciii), labeled as region 1 in Figure 7c (04:15–04:20 UTC; altitude 1,500–1,800 m). The PID classification agreed with the in situ data, also showing SLW. The presence of the stratiform layer can be attributed to dry air and a capping inversion at the top of the BL preventing further cloud growth upwards (Figure 7civ).

Figure 7d shows variations in the vertical structure within the convective cell of region 2. SLW at cloud top is a reasonable assumption if the SLW identified at 04:19 UTC and a height of 1,700 m is extrapolated to time periods during the identified convective cell. Small ice is seen beginning around 200 m below cloud top, suggesting significant ice production first starts there. The appearance of "large ice" only 100 m further below suggests a rapid increase in ice crystal size and concentration, consistent with SIP by rime splintering. It is likely that frozen precipitation was present below cloud. Since the stratiform regions were mainly liquid phase, it appears that the convective activity acted to enhance SIP processes.

The most convective of the four examples is shown in Figure 8. The cloud varies from 1,000 to 1,500 m in thickness (assuming cloud base is between 1,000 and 1,200 m, based on the lowest LWC values >0.01 g m^{-3} in Figure 8cii), compared to average thicknesses of 150, 650 and 1,200 m in the prior 3 examples. This cloud occurred around 58°S, near the center of the low pressure system seen in Figure 8a. The presence of convection is suggested by the patchiness of the clouds in the surrounding region. The ECCO-V classification (Figure 8b) shows a couple of large convective cells in the flight path, with regions of stratiform cloud in between.

Three regions are labeled in the in situ data in Figure 8c. Region 1 falls in a stratiform region according to the ECCO-V, extending from 03:37 to 03:38 UTC, with cloud top around 2,400 m, and cloud base unknown due to lack of data. Region 2, extending from 03:35 to 03:36 UTC, is within a convective region, consistent with the presence of a top overshooting the BL at about 03:35 UTC. The region extends vertically from the localized top around 2,700 m to at least 1,200 m based on the LWC seen in the in situ data, although it is not clear if cloud base is right at 1,200 m as the aircraft appears to have entered the cloud from the side, rather than from below. In region 3, from 03:32 to 03:34 UTC, the aircraft was below-cloud, shown by a lack of LWC in situ; cloud base was likely between 1,000 and 1,200 m based on elevated LWC readings at 1,200 m at 03:35 UTC, while cloud top was around 2,700 m within a localized top between 03:33 and 03:34 UTC.

Figure 8ci indicates peak 2D-S concentrations of large particles were about an order of magnitude smaller than in the last two cases (note the axis scale), although maximum LWC concentrations were similar to those in the stratiform deck displayed in Figure 6 at around 0.4 g m^{-3}. Little difference was seen between the stratiform area in region 1, and the convective area in region 2, with large variations in the LWC measured by the CDP (Figure 8cii). Concentrations of larger particles on the 2D-S did exceed 1 L^{-1} more frequently in region 2 (Figure 8ci), with these particles appearing in the form of both SLD and ice (as seen in Figures 8e and 8f). These large particles occurred alongside localized peaks in LWC, typical of convective generating cells as described in Wang et al. (2020).

Region 3 of Figures 8c and 8d designates the precipitation associated with another convective cell that the GV flew beneath. Figure 8ciii shows ice (in the form of graupel) as the dominant phase for much of this region, but shows SLW + ice around 03:34 UTC, which would more appropriately be labeled as SLD + ice based on 2D-S images from that time. With 2D-S concentrations of particles larger than 95 μm only around 1 L^{-1}, the precipitation was not very intense.

The preceding analysis indicates the presence of two convective cells of similar vertical extent (~1,500 m) and width (15–25 km) in close proximity, yet with very different phases. The PID scheme showed that ice was relatively widespread in the cell occurring within region 3, whereas the cell within region 2 contained almost exclusively SLW and SLD, with only a small amount of ice. This strong variation in the existence of different phases was frequently noted in the flight-level data during SOCRATES, and there is no clear explanation of what causes
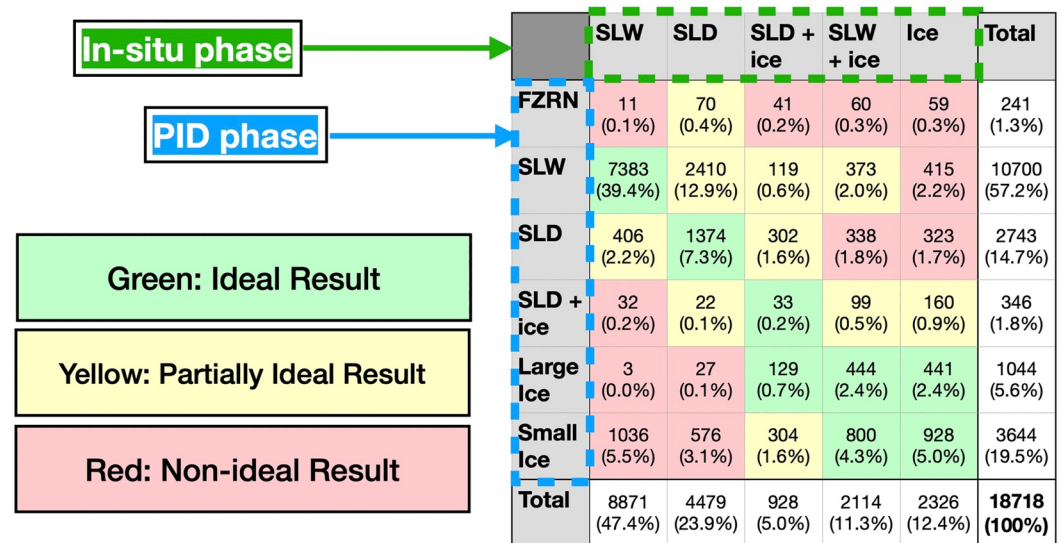
In-situ phase →

PID phase →

Green: Ideal Result

Yellow: Partially Ideal Result

Red: Non-ideal Result

	SLW	SLD	SLD + ice	SLW + ice	Ice	Total
FZRN	11 (0.1%)	70 (0.4%)	41 (0.2%)	60 (0.3%)	59 (0.3%)	241 (1.3%)
SLW	7383 (39.4%)	2410 (12.9%)	119 (0.6%)	373 (2.0%)	415 (2.2%)	10700 (57.2%)
SLD	406 (2.2%)	1374 (7.3%)	302 (1.6%)	338 (1.8%)	323 (1.7%)	2743 (14.7%)
SLD + ice	32 (0.2%)	22 (0.1%)	33 (0.2%)	99 (0.5%)	160 (0.9%)	346 (1.8%)
Large Ice	3 (0.0%)	27 (0.1%)	129 (0.7%)	444 (2.4%)	441 (2.4%)	1044 (5.6%)
Small Ice	1036 (5.5%)	576 (3.1%)	304 (1.6%)	800 (4.3%)	928 (5.0%)	3644 (19.5%)
Total	8871 (47.4%)	4479 (23.9%)	928 (5.0%)	2114 (11.3%)	2326 (12.4%)	**18718 (100%)**

Figure 9. Comparison of in situ and particle identification (PID) phase. Raw numbers of comparisons landing within each box are given, as well as percentages of the total number of measurements (18,718). For example, the red box on the top left indicates that 11 points, or 0.1% of the total number of 18,718, had freezing rain according to the PID scheme, and supercooled liquid water according to the in situ data.

these variations in phases in relatively short distances (e.g., different lifetimes of cells, role of new aerosol particle formation in causing large variations in aerosol amount (McCoy et al., 2021), etc.).

These four case studies offer a good overview of the types of BL clouds sampled during SOCRATES as relates to vertical and horizontal variability in cloud microphysical properties and cloud depths. To more thoroughly investigate the properties of such clouds, a statistical analysis of the cloud properties is performed in Section 4.

4. Comparison of In Situ and Remote Sensing Data

Before using the PID scheme to investigate the properties of SO BL clouds statistically, it is necessary to evaluate its performance against the collected in situ data. In their initial verification of the PID scheme, Romatschke and Vivekanandan (2022) found hit rates (averaged among all particle classifications) of approximately 71% during SOCRATES when compared to the in situ, collocated University of Washington Liquid-Ice Discriminator data set (Atlas et al., 2021). The following comparison procedure serves to double-check this result against the modified D'Alessandro (2021) phase product.

First, a group of PID values corresponding to the time/location of the in situ data was gathered, encompassing all range gates within 200 m of the GV's location vertically, and within 1 s of the given measurement time (i.e., the group spans an interval of 3 s). Given an airspeed near 150 ms^{-1}, this corresponds to a horizontal distance of around 450 m. A maximum of 15 valid PID retrievals will exist in the group given these dimensions and the location of the first valid bin being 107 m vertically separated from the aircraft.

Cloud phase for the group of PID values was determined as the mode of all non-null values within it. To focus the comparison on in-cloud segments, only points when the in situ cloud phase was not "out-of-cloud," and at least one non-null value existed in the group of PID values were considered. To focus on supercooled BL clouds, only locations with altitudes less than 3,000 m and temperatures less than 0°C were included. Data from flight 15 were excluded because the 2D-S did not record data. Data were also excluded if the mode of all non-null values was an unknown phase category. In total, 18,718 measurements were identified for the in situ and PID comparison, with the results shown in Figure 9.

Overall, the PID scheme shows skill in retrieving phase compared to the in situ data. Comparisons were qualitatively labeled as "ideal" (exactly matches the in situ data when considering the limitations of remote sensing data), "somewhat ideal" (one particle characteristic (size/phase) is wrong but "borders" a correct characteristic,
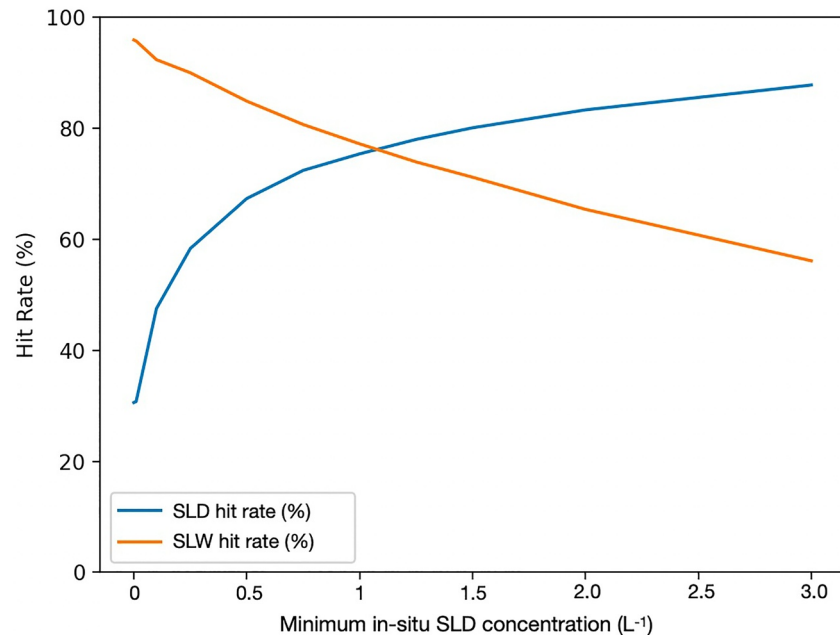
Figure 10. Sensitivity test used to find the ideal threshold of 95 μm droplets on the 2D-S probe to classify a measurement as "supercooled large drops."

e.g., mixed instead of liquid phase), and "nonideal" (one particle characteristic is wrong and does not "border" a correct characteristic, or multiple are wrong, e.g., rain instead of SLW). 11,532 (62%) of measurements landed in the green "ideal" comparison boxes, and a further 4,265 (23%) landed in the "somewhat ideal" comparison boxes, leaving a total of 2,921 (16%) in the "nonideal" boxes where the retrieved and in situ phases were very different. Using a hit rate formula of (%ideal) + 0.5*(%partially ideal) results in an effective hit rate of 73%, which is in line with the 71% hit rate from Romatschke and Vivekanandan (2022). Given uncertainty with how "partially ideal" results should be included in the hit rate, this value could fall between 62% and 85%.

Some notable areas of error do exist. For instance, despite adjusting the in situ SLD threshold to account for the sensitivity of the PID scheme (see Figure 10), 54% of in situ SLD classifications (or 13% of all compared points) were identified as SLW by the PID scheme; one reason for this may be that SLW drowns out the signal from relatively small amounts of SLD in regions with high LWC. The reverse problem was rare; only 5% of in situ SLW observations, or 2% of all comparisons, were labeled as SLD by the PID scheme.

Another area of discrepancy is that the PID category of "small ice" did not compare well to the in situ data, a phenomenon that was noted within all four case studies described in Section 3. 44% of points classified as "small ice" by the PID were SLW or SLD in the in situ data, or 9% of all points. This means that approximately half the time "small ice" was predicted by the PID scheme, the in situ phase was liquid, making it a poor predictor of phase. In contrast, only 3% of "large ice" retrievals (representing 0.1% of all comparisons) contained no ice in situ, apparently making it an effective indicator of ice presence, although confidence is limited by a small sample size.

Finally, both "FZRN" and "SLD + ice" were rare in this comparison, adding up to only 3.1% of all compared points. Perhaps due to the small sample size, neither category was very likely to indicate one particular in situ phase over any of the others, although "SLD + ice" tended to occur when the in situ phase was "SLW + ice" or "ice."

It should be noted that this comparison is likely to underestimate the accuracy of the PID scheme, due to the vertical offset of 100–150 m between the in situ observations and the first valid PID retrievals. This is an important offset given the analysis in Section 3 showed that phases and the transition from SLW to SLD often occurred over such a vertical displacement. For instance, if SLW was present at the GV's location but ice existed 100 m below, the PID scheme would be labeled as wrong in comparison to the in situ data if the scheme shows ice, even though

it would be correct considering the actual conditions; such an instance likely occurred at 04:17 UTC between 1,450 and 1,550 m elevation in Figure 7d. Thus, it appears that the PID scheme is sufficiently accurate to enable the retrieval of information about the vertical variation of phase in SO BL clouds.

Using the same comparison technique as described above, sensitivity tests using different threshold concentrations for $D > 95$ µm to identify SLD were conducted to determine the best threshold for maximizing agreement between the in situ data and PID scheme for detecting SLD. Although SLD is defined as $D > 100$ µm within the PID scheme, 95 µm is well within the margin of error for the minimum bound for SLD in the remote sensing data, allowing a comparison to be made. Probabilities of detection, or "hit rates" for SLW and SLD were calculated for situations where both the in situ and PID phase were fully liquid, ensuring that the presence or misidentification of ice did not impact the retrievals. The mean hit rate as a function of the in situ SLD threshold is shown in Figure 10. The SLW hit rate is calculated as (SLW&SLW)/(SLW&SLD + SLW&SLW), and the SLD hit rate is (SLD&SLD)/(SLD&SLW + SLD&SLD), where, for example, SLW&SLD is the number of comparisons where the PID phase is SLW and the in situ phase is SLD.

At the threshold where the SLW and SLD hit rates are the same, it is equally likely for a "SLW" retrieval from the PID to be "SLD" in situ as it is for a "SLD" retrieval from the PID to be "SLW" in situ, suggesting similar SLD detection sensitivities between the two methods. This point occurs at a concentration threshold close to 1 L^{-1}. Thus, this threshold was used to define the presence of SLD in the in situ data, even though it is approximately an order of magnitude greater than the equivalent value used by Cober and Isaac (2012). The understanding of the strengths and limitations of the PID and in situ data allow their use to determine the structure of supercooled BL clouds using the complete set of data measured during SOCRATES, as presented in the next section.

5. Typical Vertical Structure of Southern Ocean Boundary Layer Clouds

This section discusses vertical phase structures of SO BL clouds and their variability observed over the summer months during which SOCRATES was conducted. It is unknown if the typical vertical structure varies at different times of the year. This section is split into two subsections, showing average vertical cloud structure using in situ and PID phase classifications.

5.1. Vertical Structure From In Situ Data

The main uncertainty in obtaining vertical cloud phase profiles with in situ data is caused by the variability associated with the small horizontal sizes of clouds and their features (e.g., 200–600 m wide generating cells discussed by Wang et al. (2020)) and the relatively small sample size of 34 profiles obtained from the ramped ascents and descents conducted. The 34 profiles were selected by finding flight segments for which the GV flew vertically through an entire cloud, or at least a large portion of one, using areas of valid PID retrievals to help identify the location of clouds. Segments when the GV flew in-cloud at a constant altitude were not included because they provide no information about vertical variability. Clouds for which the cloud base temperature was greater than 0°C were also not included to focus on supercooled clouds. Cloud top and cloud base were defined as the topmost and bottommost elevations for which the LWC measured by the CDP was greater than 0.01 g m^{-3}. In addition, 11 out of 34 profiles had precipitation emanating from cloud base, defined by at least 10% of observations in the 500 m below cloud base having a 2D-S concentration ($D > 95$ µm) greater than 1 per liter.

In order to examine the vertical variability of phase in a common framework for all profiles, the average cloud phase was plotted as a function of the normalized altitude parameter (Z_n, McFarquhar et al., 2007) where $Z_n = 1$ for cloud top and $Z_n = 0$ for cloud base. Ten equally spaced bins for Z_n were used and separate average profiles are given for convective and stratiform clouds. For the average cloud thickness of 550 m, a change of 0.1 in Z_n is roughly a change of 55 m. This relatively large number of vertical layers is chosen to highlight phase variability at cloud top.

Figure 11 shows an example of how the in situ data were located and classified by convectivity. The small line segment, colored in teal, represents a segment of in situ phase data covering one tenth of the vertical distance between cloud base (yellow line) and cloud top (green line), which counts as one datapoint. If there are 10 in situ observations within the segment, with four identified as SLW and six identified as SLD, this datapoint would be given an averaged phase value of 40% SLW and 60% SLD. To assign the point as convective or stratiform, all echo
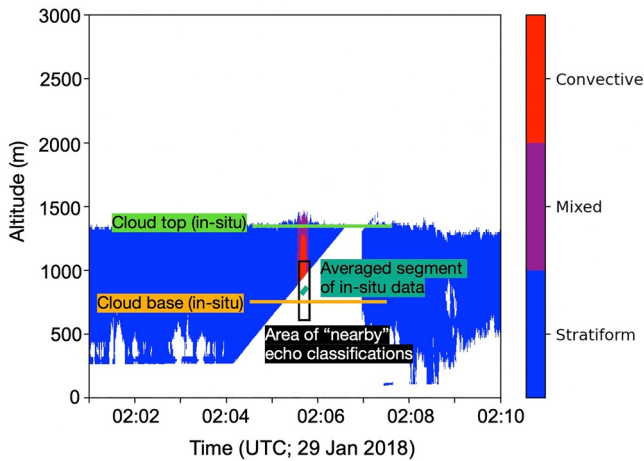
Figure 11. Illustration of data collection for the in situ vertical cloud phase classification.

classifications within 200 m vertically and 1 s in time (within around 225 m horizontally at typical aircraft velocities) of the cloud segment are retrieved (the black box in Figure 9). If at least 10% of these classifications are convective, the point is considered convective, and if at least 90% are stratiform, the point is considered stratiform. If neither of these are true, the point is not included in either the convective or stratiform data set; this can occur when a portion of echo classifications are "mixed." A lopsided percentage threshold was required due to the relative infrequency of convective clouds compared to stratiform clouds and a very small in situ data set, with no more than 34 datapoints available for each cloud layer. In this example, the datapoint would be labeled as convective, with a normalized altitude between 0.1 and 0.2.

Figure 12 shows the average vertical phase profiles from the in situ data. An additional sensitivity test with the SLD threshold as found in Cober and Isaac (2012) is included in Appendix B. For all clouds (Figure 12a), the probability of SLW (P[SLW]) was 80% at cloud top ($Z_n > 0.9$), declining to near 50% for Z_n of 0.5 and then varying less than 5% for $0 < Z_n < 0.5$. SLD was present around 10% of the time near cloud top, increasing to around 25% for $Z_n = 0.8$ and remaining relatively constant for $Z_n < 0.8$. Note that all probabilities are approximated to the nearest 5% in this discussion (denoted by ∼) due to uncertainty in the data. SLD was also present an additional ∼5% of the time when coincident with ice (SLD + ice), except at cloud top. This suggests that SLD is relatively common in SO clouds, with P[SLD or SLD + ice] ∼30% for $Z_n < 0.8$.

SLW+ice was relatively infrequent (P[SLW + ice] ∼5%–10%), for all Z_n. Ice without liquid had P[ice] ∼0 for $Z_n \geq 0.5$, increasing to ∼10% for $0.2 < Z_n < 0.3$, and returning to near zero at cloud base. However, the disappearance of ice without liquid may simply be because the cloud base was defined as the lowest altitude with CDP LWC > 0.01 g m^{-3}; hence phase at cloud base must contain liquid by definition.

Major differences in the vertical variation of phase with Z_n exist between convective (Figure 12b) and stratiform clouds (Figure 12c). Cloud top exhibited P[SLW] ∼80% regardless of convective activity. However, for $Z_n \leq 0.5$, P[SLW] was around 10% in convective clouds, compared to 60% or greater in stratiform clouds. Conversely, SLD was more frequent in convective clouds for $Z_n < 0.8$ (P[SLD] ∼35%) compared to stratiform clouds (P[SLD] ∼20%), with SLD+ice present a further ∼20% of the time in convective clouds compared to infrequently in stratiform clouds. This is consistent with the upward motion in the convective clouds being associated with the initiation of the collision-coalescence process that is necessary for the formation of SLD in these types of clouds.

A direct relationship is also seen between convective activity and ice formation. SLD + ice, SLW + ice, and ice phase were more frequent in convective clouds than in stratiform clouds. In convective clouds, a gradual increase in the presence of ice downward in cloud was noted when Z_n decreases from 1 to 0.2, with a peak P[any ice] ∼60%, with P[any ice] meaning the sum of probabilities for each ice-containing phase (SLW + ice, SLD + ice, and ice), occurring at $0.2 < Z_n < 0.5$, compared to a peak P[any ice] ∼15% in stratiform clouds (occurring at $0.0 < Z_n < 0.2$). The peak probability of a phase occurring in any single layer of the cloud is hereafter used to provide a rough estimate of the probability of observing the phase at some point within the entire cloud, which in reality is greater than or equal to this peak value.

Among the individual ice-containing phases in convective clouds, a peak is seen in the frequency of SLD + ice for $0.6 < Z_n < 0.8$, of SLW + ice for $0.4 < Z_n < 0.5$, and of ice for $0.2 < Z_n < 0.3$, with another peak in SLD + ice near cloud base ($Z_n < 0.2$). Due to the limited sample size and some uncertainties in phase identification, it is unclear the extent to which these peaks are representative of convective cloud processes in general. On the other hand, in stratiform clouds, SLW + ice retains a low probability of occurrence (∼5%) throughout the entire vertical depth of the cloud, while the probability of SLD + ice was near zero, except for $Z_n < 0.2$ ($P \sim 5\%$). Ice without any liquid was very rare in stratiform clouds.

The role of convective activity on the development of ice is consistent with past studies that have shown the role of updrafts in forming preferential environments for the production of ice in supersaturated regimes
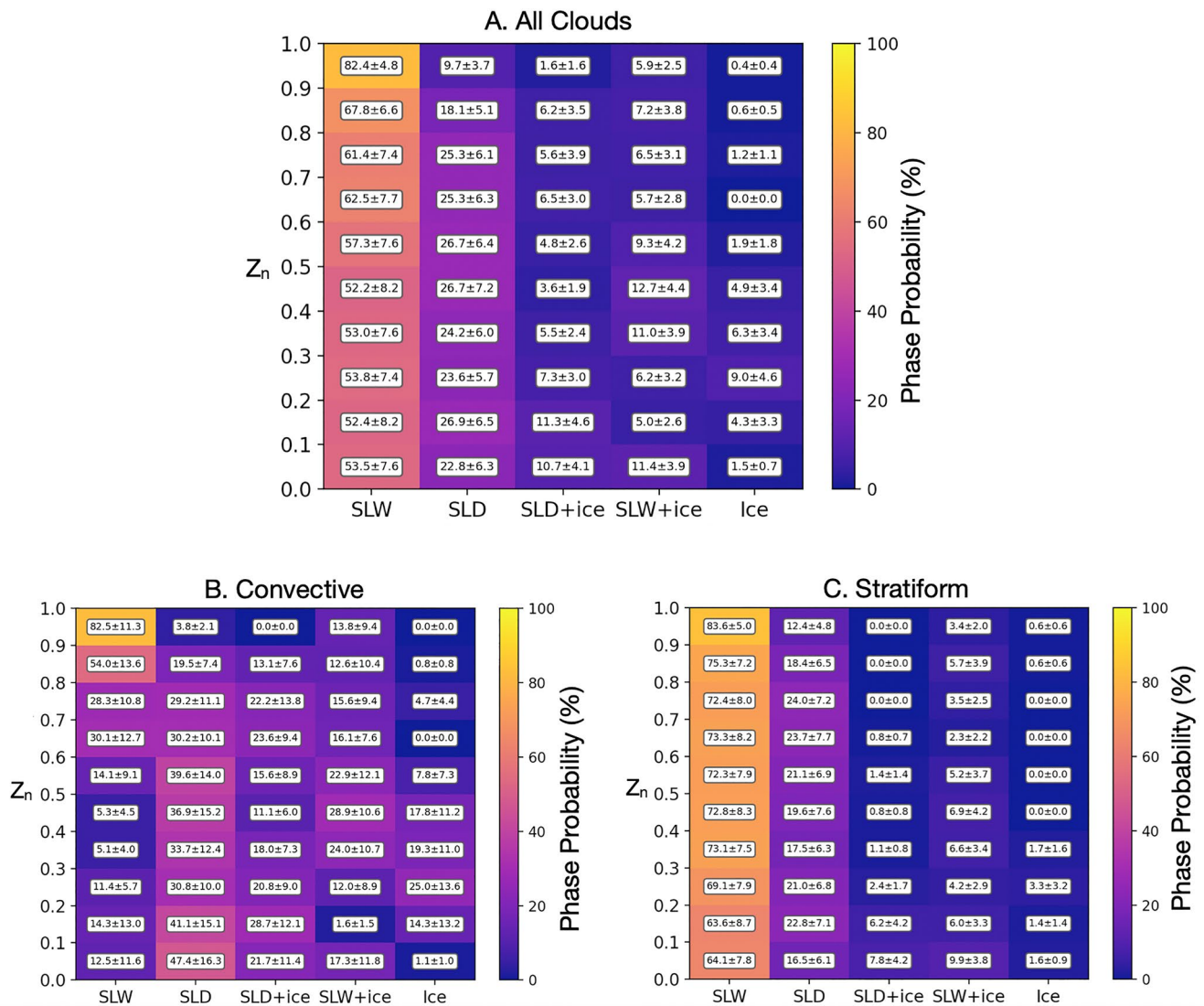
Figure 12. Average cloud phase in the vertical dimension from in situ data, using normalized altitude (Z_n).

(e.g., McFarquhar et al., 2011; Rosenow et al., 2014; Wang et al., 2020). More surprisingly, convective clouds showed more vertical heterogeneity with normalized altitude relative to stratiform clouds, considering that more vertical mixing of particles would occur within the stronger updrafts and downdrafts of convective cells, such as previously observed in the Arctic (McFarquhar et al., 2011). To extend the analysis to a larger and more representative set of data, similar analysis was conducted using the results of the PID retrievals.

5.2. Vertical Structure From PID Scheme

Vertical cloud structure was assessed using the PID scheme by isolating vertical in-cloud segments of PID retrievals. A combination of nadir and zenith-pointing retrievals were used to maximize the effectiveness of the HSRL data, which can only penetrate a few hundred meters into a cloud.

For a vertical column of nadir-facing retrievals, cloud top, if present, was considered to be the highest altitude in the column with two consecutive "in-cloud" retrievals. If the first two valid bins beneath the GV were "in-cloud," however, the data were excluded, as the location of the data relative to cloud top is unknown in these cases. Data were also excluded for clouds with tops above 3,000 m.

For zenith-facing retrievals, cloud top was defined as the topmost two consecutive "in-cloud" retrievals below 3,000 m if any cloud was present. If a cloud was present at 3,000 m, the data were not included.

For all retrievals, data were sorted into 40 bins below cloud top, with each bin representing 19 m corresponding to the vertical resolution of the PID retrievals. If there were fewer than 40 valid retrievals, all were used. This corresponds to about 750 vertical meters, and is chosen in order to be close to the average in situ average cloud thickness of 550 m for comparison, but skewed larger in order to obtain more information on the structure of deeper convective clouds. Z_n was not used for the altitude scale due to the inability to distinguish cloud base with the PID scheme.

Each valid PID value was added to a running tally of phase observations for each vertical cloud layer. Since not all data columns had 40 valid retrievals, the total number of data varied from one cloud layer to the next, but thousands of data points were still present for all layers. The fraction of phase occurrence for each altitude below cloud top was determined as the total incidences of each PID type divided by the total number of valid retrievals in each bin, to produce normalized percentages of cloud phase frequencies. The categories "rain," "drizzle," and "cloud liquid" were not included because only subfreezing temperatures were considered, and "FZRN" was not included because it appeared on a rare enough basis to be considered negligible.

For each valid PID retrieval, ECCO-V was used to determine cloud convective activity in that location so that separate statistics could be generated for convective and stratiform clouds. If the echo type was "mixed," the value was not included in either the convective or stratiform statistics, although it was included in the statistics for all clouds. Since convectivity was checked one measurement at a time, this means that if, for instance, the convectivity was stratiform at cloud top but convective 20 bins below cloud top within one vertical column, the phase at cloud top was included in the stratiform statistics, while the Phase 20 bins below cloud top was included in the convective statistics.

The results of the PID cloud phase profiles are given in Figure 13. The vertical phase distribution for all clouds is shown in Figure 13a. SLW showed a very similar variation with height as was seen for the in situ data in terms of frequency of occurrence. SLW was most common near cloud top (P[SLW] ~80%) and decreased in frequency with altitude, but remained common (P[SLW] >40%) within 750 m below cloud top; this is close to P[SLW] ~80% near cloud top and P[SLW] ~55% at Z_n < 0.5 seen in the in situ data. SLD showed a similar vertical variation as seen with the in situ data, being least common at cloud top (P[SLD] <5%) and increasing in frequency for the first 200 m below cloud top before reaching a relatively constant value of 15%–20% below 200 m. SLD was less common than observed in situ in general, with P[SLD] <20% everywhere compared to 25% with the in situ data; one explanation is that some of the SLD is being incorrectly identified as "small ice" instead. SLD + ice showed no change in prevalence with altitude with P[SLD + ice] ~5%, similar to trends in the in situ data. Small ice, which would be most comparable to "SLW + ice" or "ice" in situ, occurred throughout the depth of the cloud, but increased in frequency from cloud top (P[small ice] ~20%) to 200 m below cloud top (P[small ice] ~35%). Large ice increased steadily in frequency with decreasing altitude from cloud top (P[large ice] ~0%) to 750 m below top (P[large ice] ~20%). This shows that the clouds were increasingly glaciated with decreasing altitude. This trend was visible in situ as well, but only weakly.

As with the in situ data, major differences are present between convective (Figure 13b) and stratiform (Figure 13c) clouds. SLW was about equally likely (P[SLW] ~75%) at cloud top for convective and stratiform clouds, but quickly declined in frequency to ~5% 300 m below cloud top for convective clouds. In stratiform clouds, P[SLW] declined only slightly with altitude, reaching a relatively constant value of around 70%. SLD was rare at cloud top for both convective and stratiform clouds, but more common in general for convective clouds with a slight peak in P[SLD] ~35% 100 m below cloud top, with a relatively constant frequency of 25%–30% 150–750 m below in agreement with the in situ data. In stratiform clouds, SLD peaked in frequency at ~15% ~400 m below top. SLD + ice generally occurred at a low but nonzero frequency everywhere in both cloud types, and was slightly more frequent in the convective cases.

In convective clouds, small ice showed a peak P[small ice] ~50% 200 m below cloud top. There was then a transition to large ice, increasing from near zero at cloud top to above 50% 750 m below top. While no direct comparison exists in situ for the small/large ice distinction, the peak P[any ice] of approximately 70%, shows general agreement with the in situ data, with peak P[any ice] ~60%.
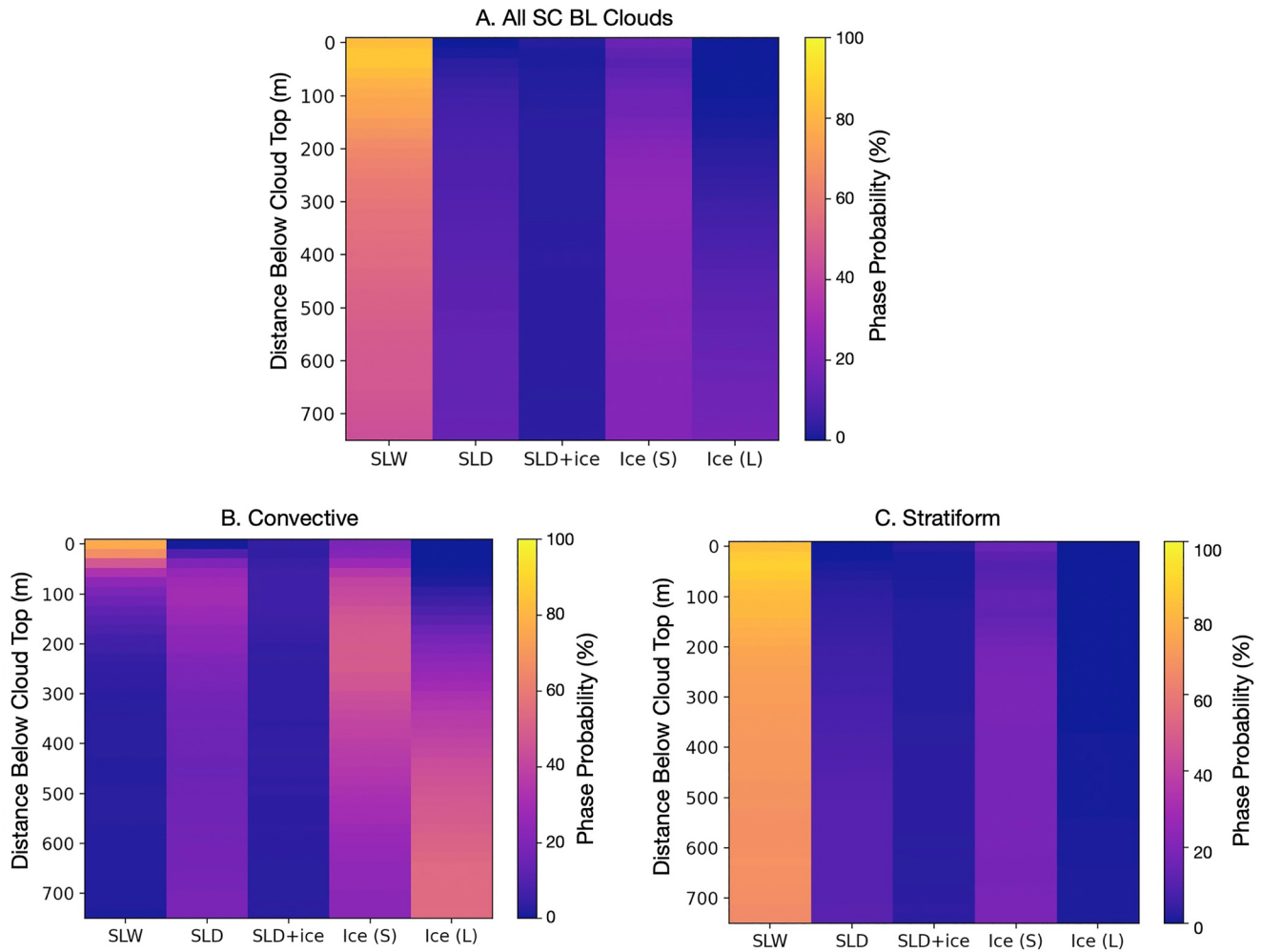
Figure 13. Average cloud phase from the particle identification scheme, using cloud top adjusted altitude.

Much less ice was observed in stratiform clouds, with large ice virtually nonexistent. Stratiform clouds had P[small ice] ~15% from 0 to 150 m below cloud top, and P[small ice] ~30% for 150–300 m below, resulting in about double the probability of ice being present than in the in situ data (peak P[any ice] ~30%, compared to peak P[any ice] ~15% for the in situ data). It is likely that some or all of this increase is due to errors in the PID scheme, as evidenced by the overestimation of ice in the in situ/PID comparison shown in Figure 9, and the patches of erroneous small ice within a general region of unknown phase in Figures 6d and 8d. Thus, SLW and SLD are likely more common than suggested by the PID scheme. It was also noted that there was a large difference between the nadir and zenith-pointing retrievals, which gives evidence that there are uncertainties in the PID retrievals causing the differences from the in situ data. The limitations of the HSRL in penetrating thick clouds is responsible for much of the difference between nadir and zenith-pointing retrievals; these limitations also cause thick clouds to be underrepresented in the PID phase statistics. For instance, among all clouds, there was P[SLW] ~30% 700 m below cloud top in the nadir-facing retrievals, compared to P[SLW] ~60% for the zenith-facing retrievals. The differences between the nadir and zenith-facing retrievals are further detailed in Appendix C.

Some differences in the results between the in situ and remote sensing data can also be attributed to the fact that the cloud base is frequently farther than 750 m from cloud top in convective clouds, meaning that cloud base is not included in the remote sensing profile at all. Further, the in situ data may be biased because the GV avoided areas where large concentrations of SLD were anticipated, likely due to strong radar returns. In addition to SLD,

these areas likely contained large ice crystals and frozen precipitation in many cases, which would lead to both SLD and ice being underrepresented by the in situ observations.

6. Conclusions

An extensive set of airborne in situ and remote sensing data were acquired during the SOCRATES. Data from the CDP, the airborne PHIPS, the RICE, and the Two-Dimensional Stereo Probe (2D-S) were used to identify cloud phase in situ, while a PID scheme applied to the HCR and High-Resolution Spectral Lidar was used to classify cloud phase from the remote sensing data. Cloud phase was generally classified as supercooled liquid water (SLW; $D < 95$ μm), supercooled large droplets (SLD; $D > 95$ μm), ice, or some combination thereof; the PID scheme also had separate classifications for small and large ice.

A comparison of the results of the PID scheme to phase identified from the in situ observations within SO BL clouds indicated an agreement rate exceeding 70%, comparable to previous evaluation of the PID scheme (Romatschke & Vivekanandan, 2022). Discrepancies between the PID scheme and the in situ observations include an underestimation of SLD (SLD was only about half as frequent in the PID scheme as in the in situ data), and an overabundance of ice (about half of "small ice" classifications were liquid phase in situ; though "large ice" compared well). However, it is possible that these discrepancies will be lessened or eliminated if the areas of unknown phase can be classified using other available remote sensing parameters in areas without LDR or LLDR data. The results of the comparison are generally quite favorable, especially considering that some of the discrepancies are due to a 100–150 m vertical gap between the in situ observations and the PID retrievals due to the dead zone of the remote sensors. Overall, the PID scheme proved useful as a means of expanding the available data set for assessing vertical cloud structure.

In situ and PID phase classifications were used to assess the average vertical phase structure of SO BL clouds, plotted as a function of normalized altitude (Z_n) for in situ data (McFarquhar et al., 2007), and as a function of distance below cloud top for PID retrievals. A much larger sample of vertical cloud phase observations was obtained from PID data than from the in situ data. However, the in situ data are useful for evaluating the PID retrievals because they are based on higher resolution observations, showing the two data streams can be used synergistically. When summarizing conclusions, it can be assumed that general agreement between the PID retrievals and the in situ phase occurred unless explicitly stated otherwise. Among all SO BL clouds, the following features were identified:

1. SLW was found to be most frequent at cloud top (P[SLW] >75%), with ice rather rare (P[any ice] <15%). SLW decreased in frequency below cloud top, declining to P[SLW] ~50% at $Z_n < 0.5$, corresponding to about 300 m below cloud top for an average thickness of 550 m. This decrease of SLW below cloud top has previously been seen in simulations (Morrison et al., 2010) and remote sensing retrievals (Zaremba et al., 2020).
2. SLD was uncommon at cloud top but became increasingly likely in the 300 m below cloud top, with in situ data indicating P[SLD] ~25% at Z_n of 0.5, and PID observations showing P[SLD] ~15%–20% at 300 m (analogous to a Z_n of 0.5). SLD + ice was present a further ~5% of the time at a Z_n of 0.5.
3. Cloud glaciation increased with decreasing altitude. In situ, there was P[any ice] <10% for $Z_n > 0.9$ and P[any ice] >20% for $Z_n < 0.5$. For the PID, there was P[any ice] <20% at cloud top and P[any ice] >40% 550 m below cloud top; this also reflects a higher frequency of ice overall according to the PID.

Observations were also separated according to their convectivity using the ECCO-V product. Below, comparisons between convective and stratiform clouds are listed:

1. While SLW was very common (P[SLW] >75%) at cloud top for both convective and stratiform clouds, it became very infrequent (P[SLW] <10%) 250 m below cloud top for convective clouds, compared to a much larger P[SLW] >50% throughout cloud depth for stratiform clouds.
2. For convective clouds, P[SLD] increased from near zero at cloud top to above 30% 200 m below cloud top. Below 200 m, the PID showed a subsequent decrease to P[SLD] ~25% 300 m below cloud top, but the in situ data had P[SLD] >30% for all $Z_n < 0.7$ (150 m below cloud top), reaching as high as 45% near cloud base. The in situ data also showed P[SLD + ice] ranging from 10% to 30%. Stratiform clouds had P[SLD] ~20% except at cloud top (P[SLD] ~10%), in situ, with P[SLD] 5%–10% lower throughout according to the PID scheme. Both methods suggest that the peak P(SLD) is 1.5–2 times larger in convective clouds.

3. There was a connection observed between convective activity and ice presence. The PID scheme showed more ice than the in situ data at all altitudes, although this is likely at least partially due to a known overabundance of small ice in the PID as seen from a comparison for the collocated data (discussed in Section 4). In stratiform clouds, there was P[any ice] ~15% at cloud top and P[any ice] ~30% below 200 m from cloud top, with virtually all of this in the form of "small ice." Rates of ice-containing phases were much larger in convective clouds with P[any ice] ~20% at cloud top, increasing to P[any ice] ~70% 250 m below. Further, the PID scheme suggests ice growth occurs with decreasing altitude in convective clouds, with P[large ice] ~10% 150 m below cloud top and P[large ice] ~50% 700 m below cloud top. This is consistent with previous studies that have shown higher updraft velocities provide a preferential environment for the growth of ice in supersaturated regimes (McFarquhar et al., 2011; Rosenow et al., 2014; Wang et al., 2020), and that SIP during SOCRATES was enhanced in convective regions exhibiting multiple updrafts (including embedded convective elements within stratocumulus clouds), with thin stratiform clouds with a lack of significant updraft activity exhibiting little SIP and remaining mostly composed of SLW (Järvinen et al., 2022; Lasher-Trapp et al., 2021; Mace et al., 2021). The peak P[any ice] for any part of the cloud averaged among both methods is ~65% for convective clouds and ~20% for stratiform clouds, suggesting that ice is about 3 times more likely in convective clouds than in stratiform clouds. In the ~25%–45% of cases with little or no ice in convective clouds, SLD was virtually always present at 150 m or more below cloud top, suggesting that collision-coalescence is an efficient process in these convective regimes.

4. Averaged vertical cloud structure profiles revealed convective clouds to be more vertically heterogeneous than stratiform clouds, with SLW at cloud top giving way to SLD or ice within 150 m below top, and continuing growth of ice crystals with further altitude decrease in the 50%–70% of cases with ice present. In contrast, SLW was present more than 60% of the time at all heights for stratiform clouds. These results suggest a stronger dependence of cloud phase in convective clouds with height than noted by McFarquhar et al. (2007, 2011), and is a surprising finding given that convective generating cells tend to produce strong turbulent mixing that would be expected to homogenize phase in the vertical dimension.

Many avenues exist for future work. For instance, the analysis in this study was restricted to the assumption that a single cloud layer was present, even though multiple cloud layers commonly exist over the SO. Further study is needed to determine the effects of these multiple cloud layers on vertical structure. In addition, the amount of in situ data used here is limited because only 15 flights over a 6-week period in a small geographic area were available. Although these data are insufficient to thoroughly investigate seasonal and spatial variations in the vertical profile structure, they still represent a first of a kind set of data giving unique characterizations of the vertical structure of clouds in this region. However, more data of this type is still needed to better characterize the dependence of cloud structure on environmental and aerosol conditions. A comparison of the structure and properties of these SO clouds to those obtained in polar regions of the NH is of interest, such as those obtained during the Indirect and Semi-Direct Aerosol Campaign (McFarquhar et al., 2011) and the recent Multidisciplinary drifting Observatory for the Study of Arctic Climate expedition. Further, the competing effects of variations in aerosol properties and vertical velocities on the distribution of phase need to be better determined. The consistency between the in situ measurements and the PID retrievals suggests that the remote sensing data are sufficiently robust to perform such a study. Finally, the attenuation of the HCR and HSRL in thick clouds makes the retrieval of cloud phase challenging. Nevertheless, these new findings on vertical cloud structure represent an important data set that can be used for the evaluation of models of SO clouds, by comparing model simulated vertical cloud phase structure to the results described here.

Appendix A: 2DC Versus 2D-S Data Comparison for RF08

Figure A1 shows the correlation between the 2DC and 2D-S probes on RF08, for concentrations of particles of sizes greater than 100, 200, 300, and 500 μm on the 2DC probe. Due to the mismatch in bin boundaries between the 2DC and the 2d-S, 2d-S concentrations use particles beginning at sizes 5 μm smaller; however, the potential error due to this bin mismatch is expected to be negligible compared to uncertainties in probe measurements (see Baumgardner et al., 2017). The slopes of the comparison lines (see the chart legend in Figure A1) between 0.5 and 0.75 indicate that the 2DC did not systematically display the erroneously high concentrations associated with fogging, which justifies the use of 2DC data for the time period where the 2D-S was not working.
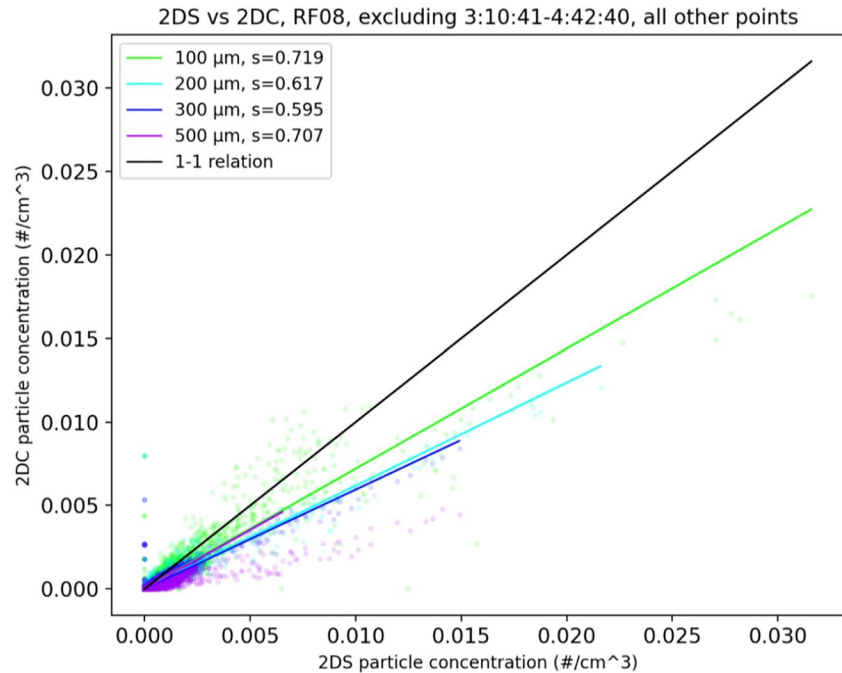
Figure A1. Comparison of 2D-S (*x*-axis) and 2D-C (*y*-axis) particle concentrations for RF08, excluding the period from 3:10:41 to 4:42:40 when the 2DS was not working correctly.

Appendix B: Sensitivity Test of 0.085 L^{-1} Droplet Concentration SLD Threshold

This section examines the impact of using different threshold concentrations of particles with $D > 95$ μm to define SLD presence. Figure B1 shows a the in-cloud phase probabilities derived from the in situ data when the Cober and Isaac (2012) threshold concentration of 0.085 L^{-1} is used to define the presence of SLD rather than the 1 L^{-1} threshold used in the main text of this paper. With this threshold, SLW frequencies decreased by about 30% for all levels of the cloud compared to at the 1 L^{-1} threshold, with this decrease more pronounced in convective clouds than in stratiform clouds. Frequencies of "SLW + ice" decreased by 10%–20% throughout convective clouds, as many observations were reclassified as "SLD + ice." A decrease of about 5% was seen for "SLW + ice" frequencies in stratiform clouds.

One particularly notable change is the frequency of SLD at cloud top ($Z_n > 0.9$) for convective clouds compared to for stratiform clouds. While SLD was seen with nearly identical probabilities (~5% for convective clouds and ~10% for stratiform clouds) at the 1 L^{-1} threshold, SLD was seen ~40% of the time in stratiform clouds and ~65% of the time in convective clouds using the 0.085 L^{-1} threshold. This suggests that SLD frequently develops in small concentrations at cloud top for convective clouds in particular, but rarely becomes very prevalent for these SO clouds. Thus, the choice of parameters used to define SLD have an impact on the findings of this study.
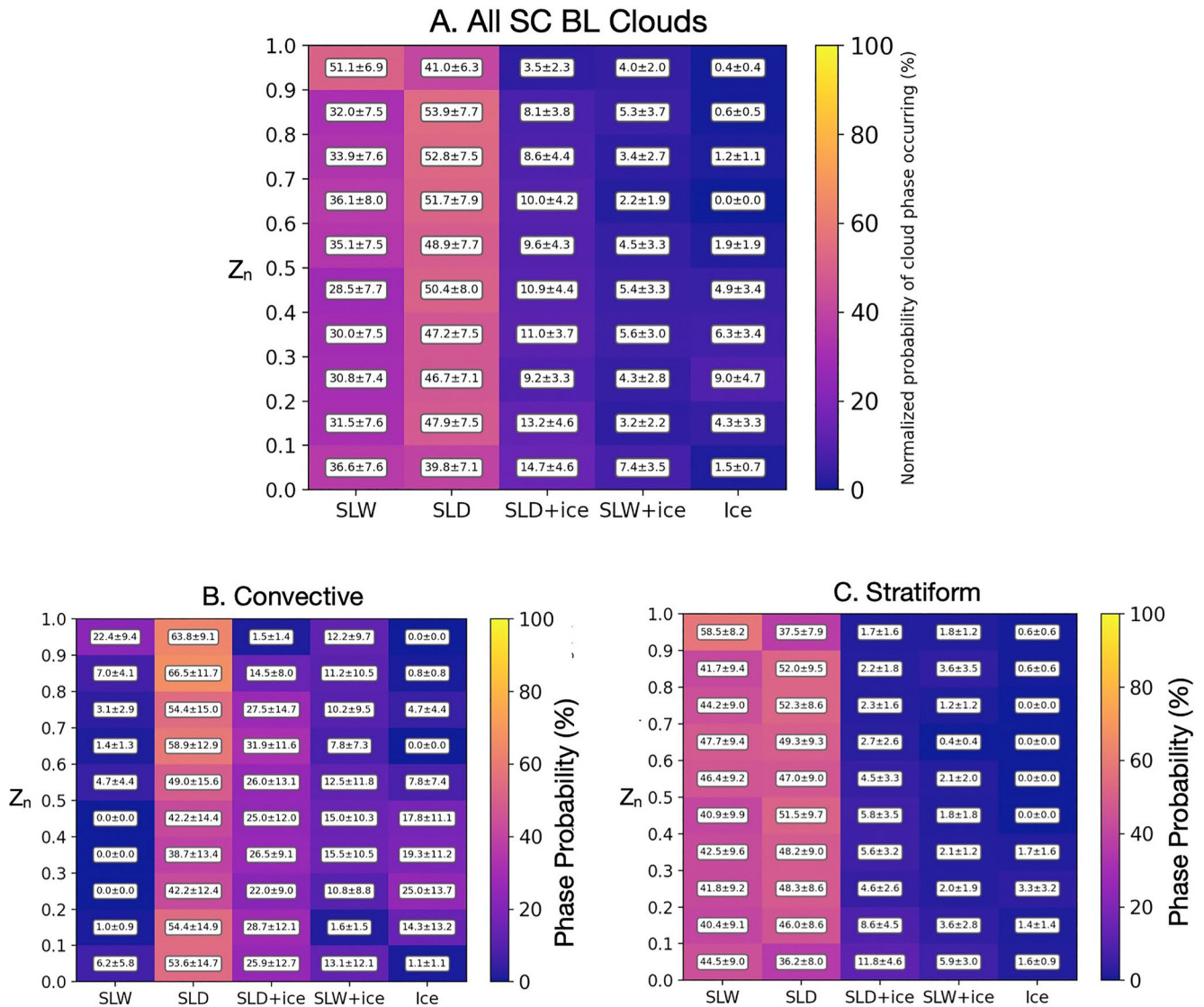
Figure B1. In situ cloud phase probabilities for 2D-S supercooled Large Droplets concentration >0.085 L^{-1}, as specified in the Cober and Isaac (2012) study.

Appendix C: Vertical Cloud Phase Profiles for Nadir and Zenith Facing PID Retrievals

Some differences in the frequency of phases from the PID scheme at cloud top and base were noted depending on whether nadir facing or zenith facing retrievals were used. Among all clouds, for the zenith-facing retrievals, SLW was about 20% less frequent 700 m below cloud top, with frequencies relatively similar compared to nadir-facing retrievals. SLD was about 15% more frequent 700 m below cloud top, and 10% less frequent 200 m below cloud top. Small ice was about 15% less frequent in the middle portions of the cloud (∼300 m below top) compared to the nadir-facing retrievals, while large ice was up to 40% less frequent 750 m below top. However, the nadir and zenith facing retrievals agree on the high frequency of SLW at cloud top to within 10%. The difference in phase fractions between the nadir and zenith facing profiles varies some for convective and stratiform clouds, but shows the same trends.

Differences between nadir and zenith pointing retrievals occur because the radar and lidar become increasingly attenuated when passing through clouds. As a result, the PID is effective at identifying relatively small SLW and
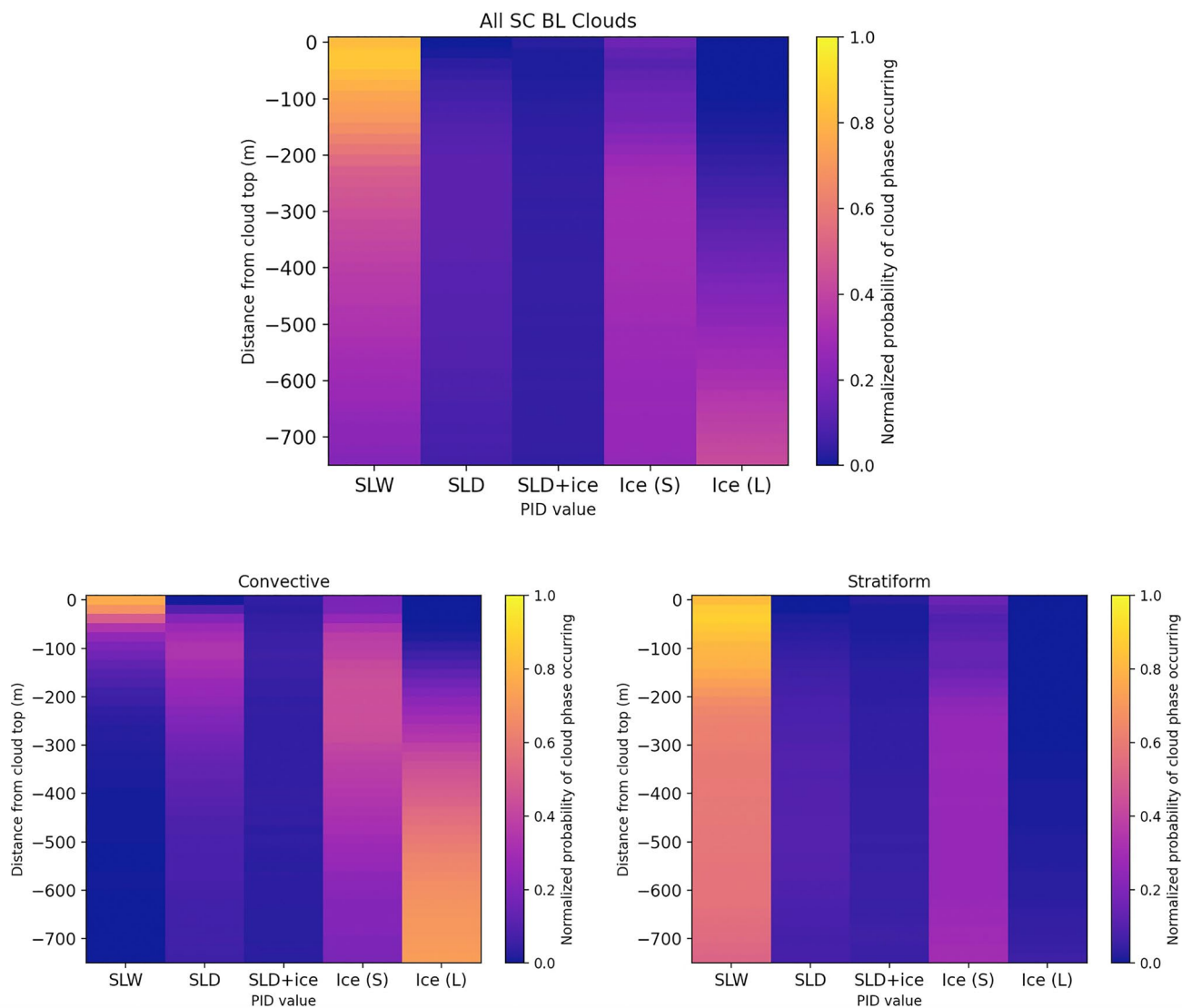
Figure C1. Average vertical cloud profile from particle identification scheme using only nadir-facing retrievals.

SLD at close range, but is often only able to distinguish the phase of the larger particles when some attenuation has occurred. For the nadir-facing retrievals, cloud top data is least attenuated, while the data closest to cloud base is least attenuated for zenith-facing retrievals Figures C1 and C2.
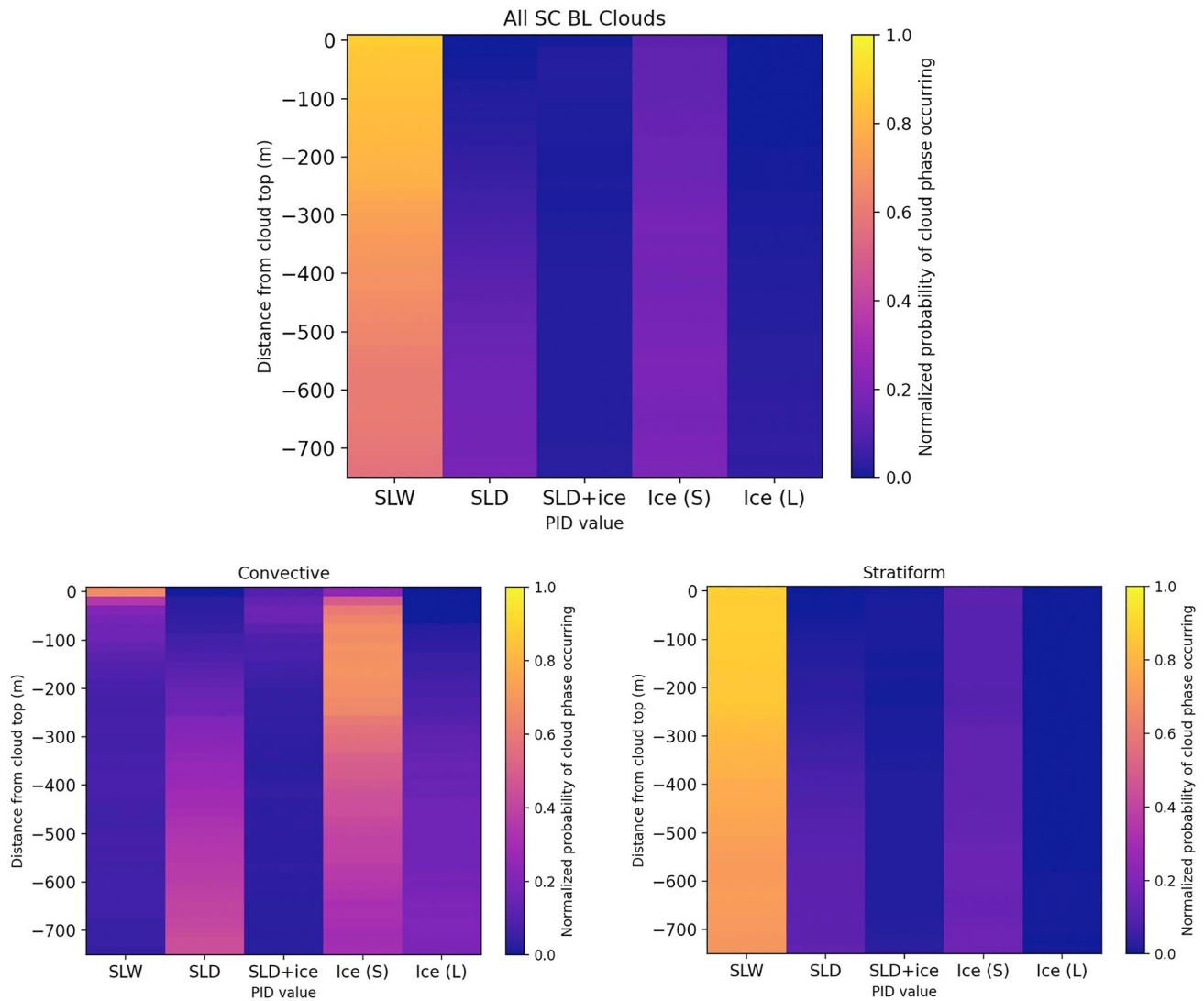
Figure C2. Average vertical cloud profile from particle identification scheme using only zenith-facing retrievals.

Data Availability Statement

Most of the data sets used in this study can be located on the EOL data archive. These data sets include the PID scheme, ECCO-V classifications, and raw remote sensing data (NCAR/EOL HCR and HSRL teams, 2022), the PHIPS images (Schnaiter, 2018), the 2D-S particle size distributions (Wu & McFarquhar, 2019), 2D-S imagery (NCAR/EOL, 2018), probe microphysics data (NCAR/EOL, 2022), and in situ phase classifications (D'Alessandro et al., 2022).

References

Abdelmonem, A., Järvinen, E., Duft, D., Hirst, E., Vogt, S., Leisner, T., & Schnaiter, M. (2016). PHIPS–HALO: The airborne particle habit imaging and polar scattering probe—Part 1: Design and operation. *Atmospheric Measurement Techniques*, *9*(7), 3131–3144. https://doi.org/10.5194/amt-9-3131-2016

Albrecht, B., Ghate, V., Mohrmann, J., Wood, R., Zudema, P., Bretherton, C., et al. (2019). Cloud System Evolution in the Trades (CSET): Following the evolution of boundary layer cloud systems with the NSF–NCAR GV. *Bulletin of the American Meteorological Society*, *100*(1), 93–121. https://doi.org/10.1175/BAMS-D-17-0180.1

Atlas, R., Mohrmann, J., Finlon, J., Lu, J., Hsiao, I., Wood, R., & Diao, M. (2021). The University of Washington Ice–Liquid Discriminator (UWILD) improves single-particle phase classifications of hydrometeors within Southern Ocean clouds using machine learning. *Atmospheric Measurement Techniques*, *14*(11), 7079–7101. https://doi.org/10.5194/amt-14-7079-2021

Baumgardner, D., Abel, S. J., Axisa, D., Cotton, R., Crosier, J., Field, P., et al. (2017). Cloud ice properties: In situ measurement challenges. *Meteorological Monographs*, *58*, 9.1–9.23. https://doi.org/10.1175/amsmonographs-d-16-0011.1

Baumgardner, D., & Rodi, A. (1989). Laboratory and wind tunnel evaluations of the Rosemount icing detector. *Journal of Atmospheric and Oceanic Technology*, *6*, 971–979. https://doi.org/10.1175/1520-0426(1989)006<0971:lawteo>2.0.co;2

Bodas-Salcedo, A., Hill, P. G., Furtado, K., Williams, K. D., Field, P. R., Manners, J. C., et al. (2016). Large contribution of supercooled liquid clouds to the solar radiation budget of the Southern Ocean. *Journal of Climate*, *29*(11), 4213–4228. https://doi.org/10.1175/jcli-d-15-0564.1

Bodas-Salcedo, A., Williams, K. D., Ringer, M. A., Beau, I., Cole, J. N. S., Dufresne, J.-L., et al. (2014). Origins of the solar radiation biases over the Southern Ocean in CFMIP2 models. *Journal of Climate*, *27*(1), 41–56. https://doi.org/10.1175/jcli-d-13-00169.1

Bony, S. (2007). Cloud radiative feedbacks in GCMs: A challenge for the simulation of climate variability and climate sensitivity. In *Proceedings of the ECMWF workshop on "Cloud parameterizations in large-scale models* (pp. 9–18). ECMWF. 11-13 Nov 2006 Retrieved from https://www.ecmwf.int/node/8279

Bony, S., Colman, R., Kattsov, V. M., Allan, R. P., Bretherton, C. S., Dufresne, J., et al. (2006). How well do we understand and evaluate climate change feedback processes? *Journal of Climate*, *19*(15), 3445–3482. https://doi.org/10.1175/jcli3819.1

Cesana, G., Waliser, D. E., Jiang, X., & Li, J.-L. F. (2015). Multimodel evaluation of cloud phase transition using satellite and reanalysis data. *Journal of Geophysical Research: Atmospheres*, *120*(15), 7871–7892. https://doi.org/10.1002/2014JD022932

Cheng, A. N., Xu, K. M., Hu, Y. X., & Kato, S. (2012). Impact of a cloud thermodynamic phase parameterization based on CALIPSO observations on climate simulation. *Journal of Geophysical Research*, *117*(D9), D09103. https://doi.org/10.1029/2011JD017263

Chubb, T. H., Jensen, J. B., Siems, S. T., & Manton, M. J. (2013). In situ observations of supercooled liquid clouds over the Southern Ocean during the HIAPER Pole-to-Pole Observation (HIPPO) campaigns. *Geophysical Research Letters*, *40*(19), 5280–5285. https://doi.org/10.1002/grl.50986

Chylek, P., & Borel, C. (2004). Mixed phase cloud water/ice structure from high spatial resolution satellite data. *Geophysical Research Letters*, *31*(14), L14104. https://doi.org/10.1029/2004GL020428

Cober, S., & Isaac, G. A. (2012). Characterization of aircraft icing environments with supercooled large drops for application to commercial aircraft certification. *Journal of Applied Meteorology and Climatology*, *51*(2), 265–284. https://doi.org/10.1175/JAMC-D-11-022.1

Cober, S. G., Isaac, G. A., & Korolev, A. V. (2001). Assessing the Rosemount icing detector with in situ measurements. *Journal of Atmospheric and Oceanic Technology*, *18*(4), 515–528. https://doi.org/10.1175/1520-0426(2001)018<0515:atridw>2.0.co;2

D'Alessandro, J., Schima, S., & McFarquhar, G. (2022). SOCRATES cloud phase product. Version 1.0 [Dataset]. UCAR/NCAR - Earth Observing Laboratory. https://doi.org/10.26023/S6WS-G5QE-H113

D'Alessandro, J. J., McFarquhar, G. M., Wu, W., Stith, J. L., Jensen, J. B., & Rauber, R. M. (2021). Characterizing the occurrence and spatial heterogeneity of liquid, ice and mixed phase low-level clouds over the Southern Ocean using in situ observations acquired during SOCRATES. *Journal of Geophysical Research: Atmospheres*, *126*(11), e2020JD034482. https://doi.org/10.1029/2020JD034482

Eloranta, E. W., Razenkov, I. A., Hedrick, J., & Garcia, J. P. (2008). The design and construction of an airborne high spectral resolution lidar. In *2008 IEEE aerospace conference* (pp. 1–6). IEEE. https://doi.org/10.1109/AERO.2008.4526390

Fan, J., Ghan, S., Ovchinnikov, M., Liu, X., Rasch, P. J., & Korolev, A. (2011). Representation of Arctic mixed-phase clouds and the Wegener-Bergeron-Findeisen process in climate models: Perspectives from a cloud-resolving study. *Journal of Geophysical Research*, *116*, D00T07. https://doi.org/10.1029/2010JD015375

Field, P. R., Lawson, R. P., Brown, P. R. A., Lloyd, G., Westbrook, C., Moisseev, D., et al. (2017). Secondary ice production: Current state of the science and recommendations for the future. *Meteorological Monographs*, *58*, 7.1–7.20. Retrieved from https://journals.ametsoc.org/view/journals/amsm/58/1/amsmonographs-d-16-0014.1.xml

Fuchs-Stone, Z., Raymond, D. J., & Sentić, S. (2020). OTREC2019: Convection over the East Pacific and Southwest Caribbean. *Geophysical Research Letters*, *47*(11), e2020GL087564. https://doi.org/10.1029/2020GL087564

Gong, X., Radenz, M., Wex, H., Seifert, P., Ataei, F., Henning, S., et al. (2022). Significant continental source of ice-nucleating particles at the tip of Chile's southernmost Patagonia region. *Atmospheric Chemistry and Physics*, *22*(16), 10505–10525. https://doi.org/10.5194/acp-22-10505-2022

Haynes, J. M., Jakob, C., Rossow, W. B., Tselioudis, G., & Brown, J. (2011). Major characteristics of Southern Ocean cloud regimes and their effects on the energy budget. *Journal of Climate*, *24*(19), 5061–5080. https://doi.org/10.1175/2011jcli4052.1

Huang, Y., Siems, S. T., Manton, M. J., Hande, L. B., & Haynes, J. M. (2012). The structure of low-altitude clouds over the Southern Ocean as seen by CloudSat. *Journal of Climate*, *25*(7), 2535–2546. https://doi.org/10.1175/jcli-d-11-00131.1. https://journals.ametsoc.org/view/journals/clim/25/7/jcli-d-11-00131.1.xml

IPCC. (2021). *Climate change 2021: The physical science basis. Contribution of working group I to the sixth assessment report of the intergovernmental panel on climate change*. In V. Masson-Delmotte, P. Zhai, A. Pirani, S. L. Connors, C. Péan, et al. (Eds.), Cambridge University Press. https://doi.org/10.1017/9781009157896

Järvinen, E., McCluskey, C. S., Waitz, F., Schnaiter, M., Bansemer, A., Bardeen, C. G., et al. (2022). Evidence for secondary ice production in Southern Ocean maritime boundary layer clouds. *Journal of Geophysical Research: Atmospheres*, *127*(16), e2021JD036411. https://doi.org/10.1029/2021JD036411

Jensen, J., & Stith, J. (2021). *Two-dimensional optical Array cloud probe (2DC)*. UCAR/NCAR - Earth Observing Laboratory. Retrieved from https://www.eol.ucar.edu/instruments/two-dimensional-optical-array-cloud-probe

Kanitz, T., Seifert, P., Ansmann, A., Engelmann, R., Althausen, D., Casiccia, C., & Rohwer, E. G. (2011). Contrasting the impact of aerosols at northern and southern midlatitudes on heterogeneous ice formation. *Geophysical Research Letters*, *38*(17), 5. https://doi.org/10.1029/2011gl048532

Kay, J. E., Bourdages, L., Miller, N. B., Morrison, A., Yettella, V., Chepfer, H., & Eaton, B. (2016). Evaluating and improving cloud phase in the Community Atmosphere Model version 5 using spaceborne Lidar observations. *Journal of Geophysical Research: Atmospheres*, *121*(8), 4162–4176. https://doi.org/10.1002/2015JD024699

Komurcu, M., Storelvmo, T., Tan, I., Lohmann, U., Yun, Y., Penner, J. E., et al. (2014). Intercomparison of the cloud water phase among global climate models. *Journal of Geophysical Research: Atmospheres*, *119*(6), 3372–3400. https://doi.org/10.1002/2013JD021119

Korolev, A., & Isaac, G. (2003). Phase transformation of mixed-phase clouds. *Quarterly Journal of the Royal Meteorological Society*, *129*(587), 19–38. https://doi.org/10.1256/qj.01.203

Lance, S., Brock, C. A., Rogers, D., & Gordon, J. A. (2010). Water droplet calibration of the Cloud Droplet Probe (CDP) and in-flight performance in liquid, ice and mixed-phase clouds during ARCPAC. *Atmospheric Measurement Techniques*, *3*(6), 1683–1706. https://doi.org/10.5194/amt-3-1683-2010

Lasher-Trapp, S., Scott, E. L., Järvinen, E., Schnaiter, M., Waitz, F., DeMott, P. J., et al. (2021). Observations and modeling of rime splintering in Southern Ocean cumuli. *Journal of Geophysical Research: Atmospheres*, *126*(23), e2021JD035479. https://doi.org/10.1029/2021JD035479

Lawson, P., O'Connor, D., Zmarzly, P., Weaver, K., Baker, B., Mo, Q., & Jonsson, H. (2006). The 2DS (Stereo) probe: Design and preliminary tests of a new airborne, high-speed, high-resolution particle imaging probe. *Journal of Atmospheric and Oceanic Technology*, *23*(11), 1462–1477. https://doi.org/10.1175/JTECH1927.1

Mace, G. G., Protat, A., & Benson, S. (2021). Mixed-phase clouds over the Southern Ocean as observed from satellite and surface based Lidar and radar. *Journal of Geophysical Research: Atmospheres*, *126*(16), e2021JD034569. https://doi.org/10.1029/2021JD034569

Mace, G. G., Zhang, Q., Vaughan, M., Marchand, R., Stephens, G., Trepte, C., & Winker, D. (2009). A description of hydrometeor layer occurrence statistics derived from the first year of merged Cloudsat and CALIPSO data. *Journal of Geophysical Research*, *114*, D00A26. https://doi.org/10.1029/2007JD009755

McCoy, D. T., Hartmann, D. L., Zelinka, M. D., Ceppi, P., & Grosvenor, D. P. (2015). Mixed-phase cloud physics and Southern Ocean cloud feedback in climate models. *Journal of Geophysical Research: Atmospheres*, *120*(18), 9539–9554. https://doi.org/10.1002/2015JD023603

McCoy, I. L., Bretherton, C. S., Wood, R., Twohy, C. H., Gettelman, A., Bardeen, C. G., & Toohey, D. W. (2021). Influences of recent particle formation on Southern Ocean aerosol variability and low cloud properties. *Journal of Geophysical Research: Atmospheres*, *126*(8), e2020JD033529. https://doi.org/10.1029/2020JD033529

McFarquhar, G., Jensen, J., & Marchand, R. (2018). *Mission report for RF08*. University Corporation for Atmospheric Research (UCAR). Retrieved from http://catalog.eol.ucar.edu/socrates/report/67/350/206925/57806949

McFarquhar, G. M., Bretherton, C., Marchand, R., Protat, A., DeMott, P. J., Alexander, S. P., et al. (2021). *Observations of clouds, aerosols, precipitation, and surface radiation over the Southern Ocean: An overview of CAPRICORN, MARCUS, MICRE and SOCRATES* (pp. 1–92). Bulletin of the American Meteorological Society. Retrieved from https://journals.ametsoc.org/view/journals/bams/aop/BAMS-D-20-0132.1/BAMS-D-20-0132.1.xml

McFarquhar, G. M., & Cober, S. G. (2004). Single-Scattering Properties of Mixed-Phase Arctic Clouds at Solar Wavelengths: Impacts on Radiative Transfer. *Journal of Climate*, *17*(19), 3799–3813. https://doi.org/10.1175/1520-0442(2004)017<3799:SPOMAC>2.0.CO;2

McFarquhar, G. M., Ghan, S., Verlinde, J., Korolev, A., Strapp, J. W., Schmid, B., et al. (2011). Indirect and semi-direct aerosol campaign. *Bulletin of the American Meteorological Society*, *92*(2), 183–201. https://doi.org/10.1175/2010bams2935.1

McFarquhar, G. M., Um, J., & Jackson, R. (2013). Small cloud particle shapes in mixed-phase clouds. *Journal of Applied Meteorology and Climatology*, *52*(5), 1277–1293. https://doi.org/10.1175/jamc-d-12-0114.1

McFarquhar, G. M., Zhang, G., Poellot, M. R., Kok, G. L., McCoy, R., Tooman, T., et al. (2007). Ice properties of single-layer stratocumulus during the mixed-phase Arctic cloud experiment: 1. Observations. *Journal of Geophysical Research*, *112*(D24), D24201. https://doi.org/10.1029/2007JD008633

Morrison, A. E., Siems, S. T., & Manton, M. J. (2011). A three-year climatology of cloud-top phase over the Southern Ocean and North Pacific. *Journal of Climate*, *24*(9), 2405–2418. https://doi.org/10.1175/2010jcli3842.1

Morrison, A. E., Siems, S. T., Manton, M. J., & Nazarov, A. (2010). A modeling case study of mixed-phase clouds over the Southern Ocean and Tasmania. *Monthly Weather Review*, *138*(3), 839–862. https://doi.org/10.1175/2009mwr3011.1

Mülmenstadt, J., Salzmann, M., Kay, J. E., Zelinka, M. D., Ma, P. L., Nam, C., et al. (2021). An underestimated negative cloud feedback from cloud lifetime changes. *Nature Climate Change*, *11*(6), 508–513. https://doi.org/10.1038/s41558-021-01038-1

NCAR/EOL HCR Team, NCAR/EOL HSRL Team. (2022). SOCRATES: NCAR HCR radar and HSRL lidar moments data. Version 3.0 [Dataset]. UCAR/NCAR - Earth Observing Laboratory. https://doi.org/10.5065/D64J0CZS

Politovich, M. K. (1989). Aircraft icing caused by large supercooled droplets. *Journal of Applied Meteorology*, *28*(9), 856–868. *JSTOR*. https://doi.org/10.1175/1520-0450(1989)028<0856:aicbls>2.0.co;2

Radenz, M., Bühl, J., Seifert, P., Baars, H., Engelmann, R., Barja González, B., et al. (2021). Hemispheric contrasts in ice formation in stratiform mixed-phase clouds (2021). Disentangling the role of aerosol and dynamics with ground-based remote sensing. *Atmospheric Chemistry and Physics*, *21*(23), 17969–17994. https://doi.org/10.5194/acp-21-17969-2021

Rauber, R. M., Ellis, S. M., Vivekanandan, J., Stith, J., Lee, W.-C., McFarquhar, G. M., et al. (2017). Finescale structure of a snowstorm over the Northeastern United States: A first look at high-resolution HIAPER cloud radar observations. *Bulletin of the American Meteorological Society*, *98*(2), 253–269. https://doi.org/10.1175/BAMS-D-15-00180.1

Romatschke, U., Dixon, M., Tsai, P., Loew, E., Vivekanandan, J., Emmett, J., & Rilling, R. (2021). The NCAR airborne 94-GHz cloud radar: Calibration and data processing. *Data*, *6*(6), 66. https://doi.org/10.3390/data6060066

Romatschke, U., & Dixon, M. J. (2022). Vertically resolved convective/stratiform echo type identification and convectivity retrieval for vertically pointing radars. *Journal of Atmospheric and Oceanic Technology*. https://doi.org/10.1175/JTECH-D-22-0019.1

Romatschke, U., & Vivekanandan, J. (2022). Cloud and precipitation particle identification using cloud radar and Lidar measurements: Retrieval technique and validation. *Earth and Space Science*, *9*(5). https://doi.org/10.1029/2022EA002299

Rosenow, A. A., Plummer, D. M., Rauber, R. M., McFarquhar, G. M., Jewett, B. F., & Leon, D. (2014). Vertical velocity and physical structure of generating cells and convection in the comma head region of continental winter cyclones. *Journal of the Atmospheric Sciences*, *71*(5), 1538–1558. https://doi.org/10.1175/jas-d-13-0249.1

Schnaiter, M. (2018). PHIPS-HALO Stereo imaging data. Version 1.0 [Dataset]. UCAR/NCAR - Earth Observing Laboratory. https://doi.org/10.5065/D62B8WWF

Schwartz, M. C., Ghate, V. P., Albrecht, B. A., Zuidema, P., Cadeddu, M. P., Vivekanandan, J., et al. (2019). Merged cloud and precipitation dataset from the HIAPER-GV for the cloud system evolution in the trades (CSET) campaign. *Journal of Atmospheric and Oceanic Technology*, *36*(6), 921–940. https://doi.org/10.1175/JTECH-D-18-0111.1

Shupe, M. D. (2007). A ground-based multisensor cloud phase classifier. *Geophysical Research Letters*, *34*(22), L22809. https://doi.org/10.1029/2007GL031008

Silber, I., Fridlind, A. M., Verlinde, J., Ackerman, A. S., Chen, Y.-S., Bromwich, D. H., et al. (2019). Persistent supercooled drizzle at temperatures below −25°C observed at McMurdo station, Antarctica. *Journal of Geophysical Research: Atmospheres*, *124*(20), 10878–10895. https://doi.org/10.1029/2019JD030882

Stephens, G. L. (2021). The cooling of light rains in a warming world. *Nature Climate Change*, *11*(6), 468–470. https://doi.org/10.1038/s41558-021-01056-z

Storelvmo, T., Kristjánsson, J. E., Lohmann, U., Iversen, T., Kirkevåg, A., & Seland, Ø. (2008). Modeling of the Wegener–Bergeron–Findeisen process—Implications for aerosol indirect effects. *Environmental Research Letters*, *3*(4), 045001. https://doi.org/10.1088/1748-9326/3/4/045001

Storelvmo, T., & Tan, I. (2015). The Wegener-Bergeron-Findeisen process—Its discovery and vital importance for weather and climate. *Meteorologische Zeitschrift*, *24*(4), 455–461. https://doi.org/10.1127/metz/2015/0626

Tan, I., & Storelvmo, T. (2016). Sensitivity study on the influence of cloud microphysical parameters on mixed-phase cloud thermodynamic phase partitioning in CAM5. *Journal of the Atmospheric Sciences*, *73*(2), 709–728. https://doi.org/10.1175/jas-d-15-0152.1

Tan, I., Storelvmo, T., & Zelinka, M. D. (2016). Observational constraints on mixed-phase clouds imply higher climate sensitivity. *Science*, *352*(6282), 224–227. https://doi.org/10.1126/science.aad5300

Trenberth, K. E., & Fasullo, J. T. (2010). Simulation of present-day and twenty-first-century energy budgets of the southern oceans. *Journal of Climate*, *23*(2), 440–454. https://doi.org/10.1175/2009JCLI3152.1

UCAR/NCAR—Earth Observing Laboratory. (2018). NSF/NCAR GV HIAPER raw 2D-S imagery. Version 1.0 [Dataset]. UCAR/NCAR Earth. https://doi.org/10.26023/8HMG-WQP3-XA0X

UCAR/NCAR—Earth Observing Laboratory. (2022). SOCRATES: Low rate (LRT - 1 sps) navigation, state parameter, and microphysics flight-level data. Version 1.4 [Dataset]. UCAR/NCAR Earth. https://doi.org/10.5065/D6M32TM9

Vergara-Temprado, J., Miltenberger, A. K., Furtado, K., Grosvenor, D. P., Shipway, B. J., Hill, A. A., et al. (2018). Strong control of Southern Ocean cloud reflectivity by ice-nucleating particles. *Proceedings of the National Academy of Sciences*, *115*(11), 2687–2692. https://doi.org/10.1073/pnas.1721627115

Vial, J., Dufresne, J. L., & Bony, S. (2013). On the interpretation of inter-model spread in CMIP5 climate sensitivity estimates. *Climate Dynamics*, *41*(11–12), 3339–3362. https://doi.org/10.1007/s00382-013-1725-9

Vivekanandan, J., Ellis, S., Tsai, P., Loew, E., Lee, W. C., Emmett, J., et al. (2015). A wing pod based millimeter wavelength airborne cloud radar. *Geoscientific Instrumentation, Methods and Data Systems*, *4*(2), 161–176. https://doi.org/10.5194/gi-4-161-2015

Waitz, F., Schnaiter, M., Leisner, T., & Järvinen, E. (2021). Phips-halo: The airborne particle habit imaging and polar scattering probe-part 3: Single-particle phase discrimination and particle size distribution based on the angular-scattering function. *Atmospheric Measurement Techniques*, *14*(4), 3049–3070. https://doi.org/10.5194/amt-14-3049-2021

Wang, Y., McFarquhar, G. M., Rauber, R. M., Zhao, C., Wu, W., Finlon, J. A., et al. (2020). Microphysical properties of generating cells over the Southern Ocean: Results from SOCRATES. *Journal of Geophysical Research: Atmospheres*, *125*(13), e2019JD032237. https://doi.org/10.1029/2019JD032237

Wu, W., & McFarquhar, G. (2019). NSF/NCAR GV HIAPER 2D-S particle size distribution (PSD) product data. Version 1.1 [Dataset]. UCAR/NCAR Earth. https://doi.org/10.26023/8HMG-WQP3-XA0X

Zaremba, T., Rauber, R., Mcfarquhar, G., DeMott, P., D'Alessandro, J., & Wu, W. (2021). Ice in Southern Ocean clouds with cloud top temperatures exceeding −5°C. *Journal of Geophysical Research: Atmospheres*, *126*(14). https://doi.org/10.1029/2021JD034574

Zaremba, T. J., Rauber, R. M., McFarquhar, G. M., Hayman, M., Finlon, J. A., & Stechman, D. M. (2020). Phase characterization of cold sector Southern Ocean cloud tops: Results from SOCRATES. *Journal of Geophysical Research: Atmospheres*, *125*(24), e2020JD033673. https://doi.org/10.1029/2020JD033673